

Synthesizing Redundancy Resolution Criteria of the Human Arm Posture in Reaching Movements

Zhi Li, Hyunchul Kim, Dejan Milutinović, and Jacob Rosen

Abstract. The aim of this work is to characterize the regularity and variability of human arm movements. The arm posture is quantified by a swivel angle that is experimentally measured when a healthy subject is reaching for targets in a spherical workspace. It is shown that without specific instruction, a subject moving his/her arm tends to use a consistent arm posture with small variations when reaching the same target position, regardless of whether the subject is moving toward or away from the target. This observed posture consistency indicates that human motor control chooses a unique arm posture associated to a 3D hand position. From the perspective of posture consistency, this work further examines the posture predictions based on two hypotheses on human arm control strategies: one that maximizes the movement efficiency towards the head, particularly toward the mouth; and the other that minimizes the power consumption in joint space. The arm posture predictions based on these two control strategies are compared and the prediction errors for each control strategy are analyzed.

1 Introduction

The study of human arm movements is complex due to the kinematic redundancy in the human arm. The human arm processes seven degrees of freedom (DOFs)

Zhi Li · Hyunchul Kim · Dejan Milutinović · Jacob Rosen
University of California, Santa Cruz, 1156 High Street, Santa Cruz, CA 95064, USA.
Bionics lab at UCSC
e-mail: {zhil, dejan}@soe.ucsc.edu,
hyunchul78@gmail.com,
rosen@ucsc.edu
<http://bionics.soe.ucsc.edu/>

while tasks in three-dimensional (3D) space only require six DOFs to be specified. A healthy human motor system provides natural resolutions to the inverse kinematics of the arm, with its control of the extra DOF outperforming that of wearable robotic arms (e.g., upper limb exoskeletons). Existing research has been focused on characterizing human arm movements in order to reveal a control strategy of the healthy human motor system, and to facilitate the design and control of upper limb exoskeletons. Enhanced synergy between the human arm and upper limb exoskeletons is expected to benefit applications such as the rehabilitation of stroke patients via upper limb exoskeletons [39, 25].

1.1 Characteristics of Human Arm Movements

Research on the characterization of human arm movements falls into two categories: from the perspective of regularity, the movements of healthy human arms demonstrate significant similarity when completing daily-life tasks, within and across human individuals; from the perspective of variability, it has been observed that the arm movements of each human individual are not exactly the same even when repeating the same task. These characteristics, namely regularity and variability universally exist in human movement, including human arm movement. Both of them contribute to the higher performance of the human arm, compared to that of existing robotic arms.

Regularity in Human Arm Movements: For decades, continuous research efforts on the regularity of human movements intended to reveal the control strategy of the healthy human motor system. According to Donders' law, the central nervous system (CNS) chooses a unique eye orientation for each gaze direction. When applied to human arm movements, Donders' law predicts that every position of the hand in 3D space naturally corresponds to a unique posture of the arm, which can be parameterized by joint angles at the shoulder and elbow. The unique pointing direction of the human arm corresponding to a given hand position (denoted by \mathbf{r}) can be expressed by a rotation axis \mathbf{n} and a rotation angle α [17].

$$\mathbf{r} = \tan \frac{\alpha}{2} \mathbf{n} \quad (1)$$

However, there have been experimental results that contradicted Donders' law. The law is obeyed more strictly for pointing movements with straight arms than for pointing movements with less restriction. According to Soechting et al [53], the arm posture corresponding to a given hand location is not independent of its previous posture. Furthermore, it has been confirmed that Donders's law is violated in some 3D space tasks [29]. The upper arm torsion varies widely when the pointing target is specified, yet the variation of torsion can be reduced by specifying the elbow angle. Note that while Donders's law is partially valid for reaching/pointing movements, it

is generally invalidated by grasping experiments [57, 54]. Due to the limited motion range at the wrist, the posture of the upper arm is strongly affected by hand orientation and therefore the violation of Donders's law is significant. Without restricting the precise orientation of the hand, Donders' law might still be applicable to the arm motions [9].

The posture consistency in reaching movements of the human arm revealed by Donders's law results in a category of posture-based movement planning strategies. These movement planning strategies assume that there exists an optimal final posture for each target position at the end of the trajectory. This assumption contradicts the prediction of trajectory-based movement planning strategies, which may lead to various arm postures at the end of the trajectory. It was proposed that posture-based strategies plan the movements at a kinematic level, while trajectory-based strategies plan the movements at a dynamic level [43]. Other approaches of combining movement planning at kinematic and dynamic levels with the posture at the end of the trajectory are described in [18, 22]

Variability in Human Arm Movements: Variability is another universal characteristic of the motor control of human arm movements [63, 66]. Early experimental studies (e.g. recording of hammering movements by Bernstein [5]) in human motor control find that human movements do not repeat in exactly the same way for the same task, even with intention. It has been found that this variability can be used as a signature to distinguish skilled from unskilled task performance. A lower level of the variability may indicate the existence of control, while its absence may indicate diseases [34]. The redundancy in the human motor system may contribute to the variability of human movements, though it is not necessarily the source of the variability [13, 31, 59].

1.2 Redundancy Resolution Based on Performance Optimization

By controlling redundant degrees of freedom, the resolution of inverse kinematics or inverse dynamics can satisfy additional task-based constraints and/or achieve an optimized performance. Existing research has considered performance optimization from the perspectives of manipulability, energy consumption, smoothness of movement, task accuracy and control complexity. Task-based redundancy resolutions are more straightforward since the control of the extra DOFs can be generally achieved by integrating the task-dependent constraints into an augmented Jacobian matrix [7, 50, 51]. The redundancy resolutions based on performance optimization tend to be more flexible, given that there are many performance indices in consideration.

Manipulability Performance: At a singular configuration, a manipulator can only execute motion and/or resist wrenches in limited directions. Keeping the manipulator away from its singularities is convenient for task operation in general, and this can be achieved either by mechanical design and/or motion planning.

Manipulability was originally defined either as the distance from the singularity [2], or as the efficiency of velocity/force transmission [6]. The Jacobian matrix, denoted as \mathbf{J} (or the matrix $\mathbf{J}\mathbf{J}^T$ if \mathbf{J} is a lower-rectangular matrix), has been used to quantify manipulability. Singular value decomposition (SVD) can be applied to the Jacobian matrix of manipulators, in order to construct the manipulability ellipsoid [45]. Possible manipulability indices for performance optimization are mostly based on the measures of the manipulability ellipsoid. The radii of the manipulability ellipsoid are frequently considered, either for the maximum/minimum singular values, or for their ratio (e.g., condition number [3], isotropy [1]). The determinant of the Jacobian matrix or dynamic Jacobian is also considered, resulting in performance indices such as manipulability and dynamic manipulability [67, 68].

The directions of the principle axes of the manipulability ellipsoid have rarely been considered as manipulability performance indices. It is worth noting that the direction of the principle axes indicate the movement efficiency of a manipulator configuration. For a given uniform effort (measured by joint velocity) in all the applicable directions in the joint space, the most efficient movement in task space is in the direction of the major principle axis of the manipulability ellipsoid, while the least efficient movement in task space is in the direction of the minor principle axis. With regards to global manipulability, indices such as condition number, isotropy can be integrated for the measurements of the workspace [14, 27].

Energy Performance: Minimization of energy, either in joint space or task space, implies that the final arm posture depends on both the initial arm posture and the trajectory. As a consequence, the arm postures for a given 3D hand position are not unique. It has been shown that energy minimization can not account for the average behavior of the arm movement [36], of eye movements [16] and of some full-body movements (e.g., standing up from a chair [37]). However, the consideration of energy performance can not be ruled out given the effects of dynamics. Instead, it should be integrated into other performance considerations such as the smoothness of motion, which reduces energy consumption by penalizing joint torque [62, 35], muscle forces [37], or time-derivatives of end-effector acceleration (i.e. jerk) [19, 11, 60, 52].

Smoothness of Movement: The idea of optimization for the smoothness of movement was first introduced as the minimization of jerk [19, 11], to account for the straight path and bell-shaped velocity of task-space trajectories in reaching movements, as well as for trajectories of "via-point" tasks, in which the hand is instructed to pass a sequence of positions. For arbitrary arm movements, minimizing the jerk along the trajectory accurately predict the speed profile of the trajectory [60] compared to the $2/3$ power law [56, 64, 46]. The minimization of jerk has been also extended to account for movements in grasping tasks [52]. An alternative of jerk minimization in task space is to minimize the jerk in the joint space [65].

Performance optimization for the smoothness of motion can also be achieved at a dynamic level by minimizing the time-derivative of joint torque [62, 35]. This minimization also accounts for the slight asymmetry observed in some via-point tasks [62, 35], which cannot be addressed by kinematic motion strategies that ignore the nonlinear arm dynamics.

Task Accuracy: Motor noise is considered to contribute to the variance of end-effector position across repetitions of the same task. It is known that motor noise is dependent on control, with its magnitude proportional to muscle activations [58, 55, 47]. As a consequence, the choice of control signals will affect the variability of a movement.

Within an open-loop control framework, the control strategy of minimizing the variance intends to optimize a sequence of muscle activations, for reduced variances in the end-effector positions and improved task accuracy [15]. The minimum variance model produces an accurate prediction of eye movements at the level of muscle activations, yet its prediction accuracy is not clear for human arm movements. Movements with longer durations can not be addressed by minimum-variance control, since the movement variability is strongly affected by sensory feedback, which is not considered in open-loop control [44].

However, considering the universal existence of the motor noise in biological systems, it makes sense to assume that there exists a general control strategy so that the relation between a trajectory and its velocity profile can be addressed.

Control Complexity: Control strategies yield different performance in the presence of noise, even if the averaged behavior is the same [59]. Optimal feedback controllers can resolve the redundancy in real-time according to the minimum intervention principle: make no effort to correct deviations away from the average behavior unless the task performance is affected.

As demonstrated in [59], the minimal intervention principle pushes the state vector orthogonally to the redundant direction, in which performance is maintained and corresponding states are equivalent to each other. In the redundant direction, which has been quantified as an "uncontrolled manifold", the probability distribution of observed states scatters in a wider range, compared to the non-redundant direction. A wide range of behaviors [59, 5, 48, 49, 26] have provided evidence of the minimal intervention principle.

Integrating Multiple Criteria for a Better Estimation of the Arm Posture: Existing hypotheses, either working collaboratively or individually, have not been able to fully predict the natural movements of human arms. However, the integration of multiple hypotheses for better prediction can help in understanding the control strategy of natural human arm movements. In this case, the challenge of formulating a cost function is that performance indices have different units, and therefore it is not trivial to combine them in a single criterion. Having this in mind, a appropriately chosen intermediate variable may help the integration of different indices into a single criterion. As shown in [23], the swivel angle is chosen as the intermediate variable, to merge two performance indices of different units (manipulability

and energy). However, the chosen intermediate variable may have different levels of sensitivity to changes in different performance indices.

The optimization of a comprehensive cost function that integrates various types of performance indices cannot be simply extended from the optimization of a single performance index, particularly with the presence of noise and disturbance in the implementation of the movement plan [42, 11]. The optimization of a single performance index along a deterministic trajectory can be constrained by task-dependent constraints, such as end-effector position, velocity and acceleration specified for the beginning or ending state. Such constraints are not valid for stochastic problems, in which the final state is affected by noise.

2 Kinematic and Dynamic Modeling of the Human Arm

2.1 Kinematic Modeling of the Human Arm

The kinematics and dynamics of the human arm during activities of daily living (ADL) have been studied to determine specifications for exoskeleton design (Figure 1) [40][38]. Articulation of the exoskeleton is achieved by seven single-axis revolute joints which support 99% of the range of motion required to perform daily activities [40]. Three revolute joints are responsible for shoulder abduction-adduction, flexion-extension and internal-external rotation. A single rotational joint is employed at the elbow, creating elbow flexion-extension. Finally, the lower arm and hand are connected by a three-axis spherical joint resulting in wrist pronation-supination, flexion-extension, and radial-ulnar deviation. As a human-machine interface (HMI), four six-axis force/torque sensors (ATI Industrial Automation, model-Mini40) are attached to the upper arm, the lower arm, the hand and the tip of the exoskeleton [32]. The force/torque sensor at the tip of the exoskeleton allows measurement of interactions between the exoskeleton and the environment.

2.1.1 Forward Kinematics

This section derives the forward kinematics for the upper limb exoskeleton.

Base Rotation for Singularity Avoidance: The bases of the two robotic arms of the upper limb exoskeleton are rotated according to Table 1, in order to move the singularity out of the range of the daily movements of the human arm.

Table 1 Base rotation of upper limb exoskeleton

	about X-axis (θ_x)	about Y-axis (θ_y)	about Z-axis (θ_z)
Left arm	132.5°	45°	90°
Right arm	132.5°	-45°	90°



Fig. 1 The upper limb exoskeleton with seven DOFs, supporting 99% of the range of motion required to perform daily activities

The transformation matrix for base rotation can be represented as Equation (2). Note that $\sin \theta_i$ is denoted as s_i , $\cos \theta_i$ is denoted as c_i , $\sin \alpha_i$ is denoted as $s\alpha_i$, $\cos \alpha_i$ is denoted as $c\alpha_i$.

$$\begin{aligned}
 T_{base} &= Rot_x(\theta_X)Rot_z(\theta_Y)Rot_z(\theta_Z) \\
 &= \begin{bmatrix} 1 & 0 & 0 & 0 \\ 0 & c\theta_X & -s\theta_X & 1 \\ 0 & s\theta_X & c\theta_X & 1 \\ 0 & 0 & 0 & 1 \end{bmatrix} \begin{bmatrix} c\theta_Y & 0 & s\theta_Y & 1 \\ 0 & 1 & 0 & 0 \\ -s\theta_Y & 0 & c\theta_Y & 1 \\ 0 & 0 & 0 & 1 \end{bmatrix} \begin{bmatrix} c\theta_Z & -s\theta_Z & 0 & 1 \\ s\theta_Z & c\theta_Z & 0 & 1 \\ 0 & 0 & 1 & 0 \\ 0 & 0 & 0 & 1 \end{bmatrix} \quad (2)
 \end{aligned}$$

For the left arm,

$$T_{base} = \begin{bmatrix} 0.0000 & -0.7071 & 0.7071 & 0 \\ -0.6756 & -0.5213 & -0.5213 & 0 \\ 0.7373 & -0.4777 & -0.4777 & 0 \\ 0 & 0 & 0 & 1.0000 \end{bmatrix}, \quad (3)$$

for the right arm,

$$T_{base} = \begin{bmatrix} 0.0000 & -0.7071 & -0.7071 & 0 \\ -0.6756 & 0.5213 & -0.5213 & 0 \\ 0.7373 & 0.4777 & -0.4777 & 0 \\ 0 & 0 & 0 & 1.0000 \end{bmatrix}. \quad (4)$$

Denavit-Hartenberg (DH) Parameters: The Denavit-Hartenberg (DH) parameters of the upper limb exoskeleton (shown in Table 2) are derived in the standard method defined by [8].

Table 2 Denavit-Hartenberg (DH) Parameters for upper limb exoskeleton

Robot	$i-1$	i	α_i	a_i	d_i	θ_i
Left Arm	0	1	$\pi/2$	0	0	$\theta_1 + \pi - 32.94^\circ$
	1	2	$\pi/2$	0	0	$\theta_2 + \pi/2 - 28.54^\circ$
	2	3	$\pi/2$	0	0	$\theta_3 + \pi - 53.6^\circ$
	3	4	$\pi/2$	0	L_1	θ_4
	4	5	$-\pi/2$	0	0	$\theta_5 - \pi/2$
	5	6	$-\pi/2$	0	L_2	$\theta_6 + \pi/2$
	6	7	$\pi/2$	0	0	$\theta_7 + \pi$
Right Arm	0	1	$\pi/2$	0	0	$\theta_1 - 32.94^\circ$
	1	2	$\pi/2$	0	0	$\theta_2 - \pi/2 - 28.54^\circ$
	2	3	$-\pi/2$	0	0	$\theta_3 - \pi - 53.6^\circ$
	3	4	$-\pi/2$	0	$-L_1$	θ_4
	4	5	$\pi/2$	0	0	$\theta_5 + \pi/2$
	5	6	$-\pi/2$	0	$-L_2$	$\theta_6 + \pi/2$
	6	7	$\pi/2$	0	0	$\theta_7 + \pi$

Note that L_1 and L_2 are the length of the upper and lower arms, respectively.

By direct kinematics, we can derive the transformation matrix 0_7T , which includes the position and the orientation of the wrist of the exoskeleton with respect to the base frame:

$${}^base_7T = T_{base} \cdot {}^0_1T \cdot {}^1_2T \cdot {}^2_3T \cdot {}^3_4T \cdot {}^4_5T \cdot {}^5_6T \cdot {}^6_7T = \begin{bmatrix} r_{11} & r_{12} & r_{13} & P_{wx} \\ r_{21} & r_{22} & r_{23} & P_{wy} \\ r_{31} & r_{32} & r_{33} & P_{wz} \\ 0 & 0 & 0 & 1 \end{bmatrix} \quad (5)$$

For reaching movements, the three DOFs at the wrist are not considered. Therefore, the forward kinematics that involves four DOFs of the human arm (three DOFs at the shoulder and one DOF at the elbow) becomes:

$${}^base_7T = T_{base} \cdot {}^0_1T \cdot {}^1_2T \cdot {}^2_3T \cdot {}^3_4T \cdot {}^4_5T \quad (6)$$

2.1.2 Inverse Kinematics

With the specification of the transformation matrix 0_7T , the inverse kinematics of the exoskeleton can be derived for the left and the right arms, respectively. The redundant DOF of the human arm can be constrained by specifying the elbow position ($P_e = [Pe_x, Pe_y, Pe_z]^T$).

Based on shoulder position P_s , elbow position P_e , and wrist position P_w , θ_4 can be derived as:

$$W = \|P_w - P_s\| \quad (7)$$

$$c_4 = \frac{L_1^2 + L_2^2 - W^2}{2L_1L_2} \quad (8)$$

$$s_4 = \sqrt{1 - c_4^2} \quad (9)$$

$$\theta_4 = \pi - \text{Atan2}(s_4, c_4) \quad (10)$$

The transformation matrix 3_4T and its inverse ${}^3_4T^{-1}$ can be found based on θ_4 .

The transformation matrix without the base rotation, denoted ${}^7_{base}T$, can be found by:

$${}^0_7T = T_0^{-1} \cdot {}^7_{base}T = \begin{bmatrix} r'_{11} & r'_{12} & r'_{13} & 0 \\ r'_{21} & r'_{22} & r'_{23} & 0 \\ r'_{31} & r'_{32} & r'_{33} & 0 \\ 0 & 0 & 0 & 1 \end{bmatrix} \begin{bmatrix} {}^0_7P_{wx} \\ {}^0_7P_{wy} \\ {}^0_7P_{wz} \\ 1 \end{bmatrix} \quad (11)$$

Thus, the wrist position with respect to the rotated base is ${}^0_7P_w = [{}^0_7P_{wx}, {}^0_7P_{wy}, {}^0_7P_{wz}]^T$.

Similarly, the elbow position with respect to the rotated base, denoted by ${}^0_7P_e = [{}^0_7P_{ex}, {}^0_7P_{ey}, {}^0_7P_{ez}]^T$, is:

$$\begin{bmatrix} {}^0_7P_{ex} \\ {}^0_7P_{ey} \\ {}^0_7P_{ez} \\ 1 \end{bmatrix} = T_0^{-1} \cdot \begin{bmatrix} {}^{base}_7P_{ex} \\ {}^{base}_7P_{ey} \\ {}^{base}_7P_{ez} \\ 1 \end{bmatrix} \quad (12)$$

Note that ${}^0_7P_e = {}^0_4P_e$ and

$${}^0_4T = {}^0_1T \cdot {}^1_2T \cdot {}^2_3T \cdot {}^3_4T = \begin{bmatrix} {}^0_4R & {}^0_4P_{ex} \\ & {}^0_4P_{ey} \\ & {}^0_4P_{ez} \\ 0 & 0 & 0 & 1 \end{bmatrix} = \begin{bmatrix} {}^0_4R & L_1c_1s_2 \\ & L_1c_2 \\ & L_1s_1s_2 \\ 0 & 0 & 0 & 1 \end{bmatrix} \quad (13)$$

For the both arms,

$$c_2 = \frac{{}^0_4P_{ey}}{L_1} \quad (14)$$

For the left arm,

$$s_2 = \sqrt{(1 - c_2^2)} \quad (15)$$

for the right arm,

$$s_2 = -\sqrt{1 - c_2^2} \quad (16)$$

Thus, θ_2 can be resolved as:

$$\theta_2 = \text{Atan2}(s_2, c_2) - (\pi/2 - 28.54^\circ) \quad (17)$$

To resolve θ_1 , for the both arms,

$$c_1 = \frac{{}^0P_{ex}}{L_1 s_2} \quad (18)$$

$$s_1 = \frac{{}^0P_{ez}}{L_1 s_2} \quad (19)$$

Thus, for the left arm,

$$\theta_1 = \text{Atan2}(s_1, c_1) - (\pi - 32.94^\circ) \quad (20)$$

for the right arm,

$$\theta_1 = \text{Atan2}(s_1, c_1) + 32.94^\circ \quad (21)$$

The transformation matrices 0_1T and 1_2T and their inverses ${}^0_1T^{-1}$ and ${}^1_2T^{-1}$ can be found accordingly.

Thus, the wrist position with respect to Frame 2, denoted ${}^2_7P_w = [{}^2_7P_{wx}, {}^2_7P_{wy}, {}^2_7P_{wz}]^T$, can be found:

$${}^2_7T = {}^1_2T^{-1} \cdot {}^0_1T^{-1} \cdot {}^0_7T = \begin{bmatrix} {}^2_7R & {}^2_7P_{wx} \\ & {}^2_7P_{wy} \\ & {}^2_7P_{wz} \\ 0 & 0 & 0 & 1 \end{bmatrix} \quad (22)$$

For the left arm,

$${}^2_7P_w = \begin{bmatrix} -L_2 c_3 s_4 \\ -L_1 - L_2 c_4 \\ -L_2 s_3 s_4 \end{bmatrix} \quad (23)$$

for the right arm,

$${}^2_7P_w = \begin{bmatrix} -L_2 c_3 s_4 \\ -L_1 - L_2 c_4 \\ L_2 s_3 s_4 \end{bmatrix} \quad (24)$$

To resolve θ_3 , for the both arms,

$$c_3 = \frac{{}^2_7P_{wx}}{-L_2s_4} \quad (25)$$

For the left arm,

$$s_3 = \frac{{}^2_7P_{wz}}{L_2s_4} \quad (26)$$

$$\theta_3 = \text{Atan2}(s_3, c_3) - (\pi - 53.6^\circ) - 2\pi \quad (27)$$

for the left arm,

$$s_3 = \frac{{}^2_7P_{wz}}{-L_2s_4} \theta_3 = \text{Atan2}(s_3, c_3) + (\pi + 53.6^\circ) \quad (28)$$

The transformation matrix 2_3T and its inverse ${}^2_3T^{-1}$ can be found accordingly.

θ_5 , θ_6 and θ_7 can be derived from the transformation matrices from Frame 4 to Frame 7 4_7T .

$${}^4_7T = {}^3_4T^{-1} \cdot {}^2_3T^{-1} \cdot {}^1_2T^{-1} \cdot {}^0_1T^{-1} \cdot {}^0_7T = \begin{bmatrix} {}^4_7r_{11} & {}^4_7r_{12} & {}^4_7r_{13} & {}^4_7P_{wx} \\ {}^4_7r_{21} & {}^4_7r_{22} & {}^4_7r_{23} & {}^4_7P_{wy} \\ {}^4_7r_{31} & {}^4_7r_{32} & {}^4_7r_{33} & {}^4_7P_{wz} \\ 0 & 0 & 0 & 1 \end{bmatrix} \quad (29)$$

For the left arm,

$$\begin{aligned} {}^4_7T &= {}^3_4T^{-1} \cdot {}^2_3T^{-1} \cdot {}^1_2T^{-1} \cdot {}^0_1T^{-1} \cdot {}^0_7T \\ &= \begin{bmatrix} c_5c_6c_7 - s_5s_7 & -c_7s_5 - c_5c_6s_7 & c_5s_6 & 0 \\ -c_7s_6 & s_6s_7 & c_6 & L_2 \\ -c_5s_7 - c_6c_7s_5 & c_5c_7 - c_6s_5s_7 & -s_5s_6 & 0 \\ 0 & 0 & 0 & 1 \end{bmatrix} \end{aligned} \quad (30)$$

for the right arm,

$$\begin{aligned} {}^4_7T &= {}^3_4T^{-1} \cdot {}^2_3T^{-1} \cdot {}^1_2T^{-1} \cdot {}^0_1T^{-1} \cdot {}^0_7T \\ &= \begin{bmatrix} c_5c_6c_7 - s_5s_7 & -c_7s_5 - c_5c_6s_7 & c_5s_6 & 0 \\ c_7s_6 & -s_6s_7 & -c_6 & L_2 \\ c_5s_7 + c_6c_7s_5 & c_5c_7 - c_6s_5s_7 & s_5s_6 & 0 \\ 0 & 0 & 0 & 1 \end{bmatrix} \end{aligned} \quad (31)$$

Thus, for the left arm,

$$c_6 = \frac{4}{7}r_{23} \quad (32)$$

$$s_6 = \sqrt{1 - c_6^2} \quad (33)$$

$$c_5 = \frac{\frac{4}{7}r_{13}}{s_6} \quad (34)$$

$$s_5 = -\frac{\frac{4}{7}r_{33}}{s_6} \quad (35)$$

$$c_7 = -\frac{\frac{4}{7}r_{21}}{s_6} \quad (36)$$

$$s_7 = \frac{\frac{4}{7}r_{22}}{s_6} \quad (37)$$

for the right arm,

$$c_6 = -\frac{4}{7}r_{23} \quad (38)$$

$$s_6 = \sqrt{1 - c_6^2} \quad (39)$$

$$c_5 = -\frac{\frac{4}{7}r_{13}}{s_6} \quad (40)$$

$$s_5 = -\frac{\frac{4}{7}r_{33}}{s_6} \quad (41)$$

$$c_7 = -\frac{\frac{4}{7}r_{21}}{s_6} \quad (42)$$

$$s_7 = -\frac{\frac{4}{7}r_{22}}{s_6} \quad (43)$$

For the left arm,

$$\theta_5 = \text{Atan2}(s_5, c_5) + \pi/2 \quad (44)$$

$$\theta_6 = \text{Atan2}(s_6, c_6) - \pi/2 \quad (45)$$

$$\theta_7 = \text{Atan2}(s_7, c_7) - \pi + 2\pi \quad (46)$$

for the right arm,

$$\theta_5 = \text{Atan2}(s_5, c_5) - \pi/2 \quad (47)$$

$$\theta_6 = \text{Atan2}(s_6, c_6) - \pi/2 \quad (48)$$

$$\theta_7 = \text{Atan2}(s_7, c_7) - \pi + 2\pi \quad (49)$$

For reaching movements, the four DOFs in consideration (three DOFs at the shoulder and one DOF at the elbow) can be resolved based on the wrist position P_w and the elbow position P_e : θ_4 is resolved according to Equation (10); θ_1 and θ_2 are resolved according to Equations (13) to (21). With regards to θ_3 ,

For the left arm,

$${}^2_5P_w = \begin{bmatrix} -L_2c_3s_4 \\ -L_1 - L_2c_4 \\ -L_2s_3s_4 \end{bmatrix} \quad (50)$$

for the right arm,

$${}^2_5P_w = \begin{bmatrix} -L_2c_3s_4 \\ -L_1 - L_2c_4 \\ L_2s_3s_4 \end{bmatrix} \quad (51)$$

Therefore, θ_3 can be resolved as Equations (25) to (28).

2.2 Jacobian Matrix

The Jacobian matrix denotes the mapping from joint space to task space at the velocity level.

$$\dot{P}_w = J\dot{\theta} \quad (52)$$

For the seven-DOF arm model involving wrist orientation,

$$\dot{P}_w = J_{3 \times 7}\dot{\theta} \quad (53)$$

where $\theta = [\theta_1, \theta_2, \theta_3, \theta_4, \theta_5, \theta_6, \theta_7]^T$, and

$$J_{3 \times 7} = [J_1 \ J_2 \ J_3 \ J_4 \ \mathbf{0} \ \mathbf{0} \ \mathbf{0}] \quad (54)$$

The arm model for reaching movements only involves four DOFs and therefore

$$\dot{P}_w = J_{3 \times 4}\dot{\theta} \quad (55)$$

where $\theta = [\theta_1, \theta_2, \theta_3, \theta_4]^T$ and

$$J_{4 \times 7} = [J_1 \ J_2 \ J_3 \ J_4] \quad (56)$$

For the right arm, given that

$$P_w = \begin{bmatrix} L_2(s_4(s_1s_3 - c_1c_2c_3) + c_1c_4s_2) + L_1c_1s_2 \\ L_1c_2 + L_2(c_2c_4 + c_3s_2s_4) \\ L_1s_1s_2 - L_2(s_4(c_1s_3 + c_2c_3s_1) - c_4s_1s_2) \end{bmatrix} \quad (57)$$

we have

$$J_1 = \begin{bmatrix} L_2(s_4(c_1s_3 + c_2c_3s_1) - c_4s_1s_2) - L_1s_1s_2 \\ L_1c_2 + L_2(c_2c_4 + c_3s_2s_4) \\ L_2(s_4(s_1s_3 - c_1c_2c_3) + c_1c_4s_2) + L_1c_1s_2 \end{bmatrix} \quad (58)$$

$$J_2 = \begin{bmatrix} L_2(s_4(s_1s_3 + c_1c_3s_2) + c_1c_2c_4) + L_1c_1c_2 \\ -L_1s_2 - L_2(c_4s_2 - c_2c_3s_4) \\ L_1c_2s_1 - L_2(s_4(c_1s_3 - c_3s_1s_2) - c_2c_4s_1) \end{bmatrix} \quad (59)$$

$$J_3 = \begin{bmatrix} L_2(s_4(c_3s_1 + c_1c_2s_3) + c_1c_4s_2) + L_1c_1s_2 \\ L_1c_2 + L_2(c_2c_4 - s_2s_3s_4) \\ L_1s_1s_2 - L_2(s_4(c_1c_3 - c_2s_1s_3) - c_4s_1s_2) \end{bmatrix} \quad (60)$$

$$J_4 = \begin{bmatrix} L_2(c_4(s_1s_3 - c_1c_2c_3) - c_1s_2s_4) + L_1c_1s_2 \\ L_1c_2 - L_2(c_2s_4 - c_3c_4s_2) \\ L_1s_1s_2 - L_2(c_4(c_1s_3 + c_2c_3s_1) + s_1s_2s_4) \end{bmatrix} \quad (61)$$

For the left arm, given that

$$P_w = \begin{bmatrix} L_2(s_4(s_1s_3 - c_1c_2c_3) + c_1c_4s_2) + L_1c_1s_2 \\ L_1c_2 + L_2(c_2c_4 + c_3s_2s_4) \\ L_1s_1s_2 - L_2(s_4(c_1s_3 + c_2c_3s_1) - c_4s_1s_2) \end{bmatrix} \quad (62)$$

we have

$$J_1 = \begin{bmatrix} -L_2(s_4(c_1s_3 - c_2c_3s_1) + c_4s_1s_2) - L_1s_1s_2 \\ L_1c_2 + L_2(c_2c_4 + c_3s_2s_4) \\ L_1c_1s_2 - L_2(s_4(s_1s_3 + c_1c_2c_3) - c_1c_4s_2) \end{bmatrix} \quad (63)$$

$$J_2 = \begin{bmatrix} L_1c_1c_2 - L_2(s_4(s_1s_3 - c_1c_3s_2) - c_1c_2c_4) \\ -L_1s_2 - L_2(c_4s_2 - c_2c_3s_4) \\ L_2(s_4(c_1s_3 + c_3s_1s_2) + c_2c_4s_1) + L_1c_2s_1 \end{bmatrix} \quad (64)$$

$$J_3 = \begin{bmatrix} L_1c_1s_2 - L_2(s_4(c_3s_1 - c_1c_2s_3) - c_1c_4s_2) \\ L_1c_2 + L_2(c_2c_4 - s_2s_3s_4) \\ L_2(s_4(c_1c_3 + c_2s_1s_3) + c_4s_1s_2) + L_1s_1s_2 \end{bmatrix} \quad (65)$$

$$J_4 = \begin{bmatrix} L_1c_1s_2 - L_2(c_4(s_1s_3 + c_1c_2c_3) + c_1s_2s_4) \\ L_1c_2 - L_2(c_2s_4 - c_3c_4s_2) \\ L_2(c_4(c_1s_3 - c_2c_3s_1) - s_1s_2s_4) + L_1s_1s_2 \end{bmatrix} \quad (66)$$

2.3 Redundancy Representation by Swivel Angle

In addition to the elbow position, the extra degree of freedom can be constrained by specifying the swivel angle. When the arm is not straight, the positions of the

shoulder (P_s), the elbow (P_e) and the wrist (P_w) form a triangle. With the spherical joints at both the shoulder and wrist, the elbow position P_e can only rotate around the vector ($P_w - P_s$) (see Figure 2). A local coordinate system at the center of the elbow circle (P_c) gives a reference for measuring the swivel angle (ϕ) of the elbow. A normal vector that points in the direction of ($P_w - P_s$) is defined as:

$$\mathbf{n} = \frac{P_w - P_s}{\|P_w - P_s\|} \quad (67)$$

A normalized vector projected onto the plane orthogonal to \mathbf{n} is given by:

$$\mathbf{u} = \frac{\mathbf{a} - (\mathbf{a} \cdot \mathbf{n})\mathbf{n}}{\|\mathbf{a} - (\mathbf{a} \cdot \mathbf{n})\mathbf{n}\|} \quad (68)$$

where \mathbf{a} is the vector to be projected. Badler and Torlani [4] suggest that \mathbf{a} should be $[0, 0, -1]^T$. This selection has real physical meaning. When ϕ is equal to zero, the elbow is at its lowest possible point. The last vector of the coordinate system (\mathbf{v}), is found by taking the cross product of \mathbf{n} and \mathbf{u} . Vectors \mathbf{n} , \mathbf{u} and \mathbf{v} form an orthogonal coordinate system, where \mathbf{u} and \mathbf{v} are in the plane of the elbow circle (Figure 2(b)). The radius (R) and center (P_c) of the circle are easily found through geometry.

$$\cos(\alpha) = \frac{L_1^2 - L_2^2 - \|P_w - P_s\|^2}{-2L_2\|P_w - P_s\|} \quad (69)$$

$$\sin(\alpha) = \sqrt{1 - \cos(\alpha)} \quad (70)$$

$$R = L_1 \sin(\alpha) \quad (71)$$

$$P_c = P_s + L_1 \cos(\alpha) \cdot \mathbf{n} \quad (72)$$

, where L_1 and L_2 are the lengths of the upper and lower arm segments (Figure 2(a)). The position of the elbow can now be expressed as a parametrization of ϕ [61].

$$P_e = R[\cos(\phi)\mathbf{u} + \sin(\phi)\mathbf{v}] + P_c \quad (73)$$

2.4 Dynamic Modeling of the Human Arm

The dynamic models of the left and right human arms are built up by integrating the kinematic model with the estimates of mass, the center of mass and the moment of inertia. Dynamic models of the human arm are rendered via the Autolev package [12], which generates the motion equation by Kane's method [20]. Each arm model processes seven DOFs (three DOFs for the shoulder, three DOFs for the wrist and one DOF for the elbow motion), with the frame setup in accordance with the EXO-UL7. Since the analysis of reaching movements in free space does not specify the wrist posture, the orientation of the hand in the dynamic model is pre-specified by locking the three DOFs at the wrist joint.

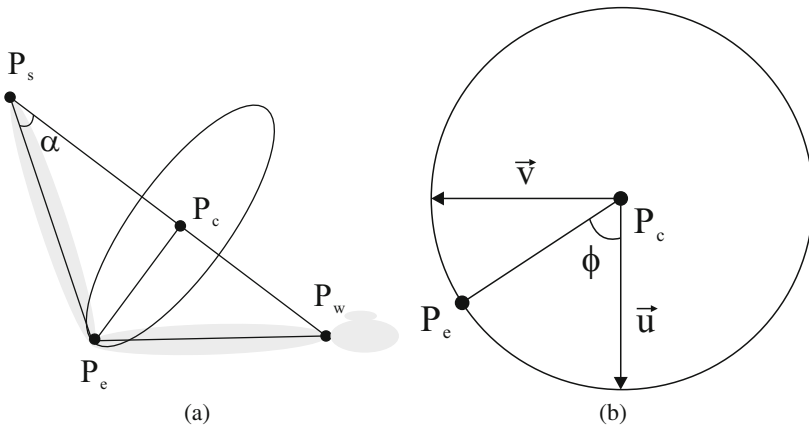


Fig. 2 Swivel angle

Given the initial condition of the human arm, the dynamic model can respond to external forces (such as gravity) and provide an analytical calculation of the joint space variables (i.e., joint angles, velocities and accelerations), as well as the kinetic energy and potential energy. The analytical calculation of joint torque is integrated in the dynamic model and can be extracted to compute work in the joint space. The dynamic model can also respond to external joint torques and generate the resulting joint space values accordingly.

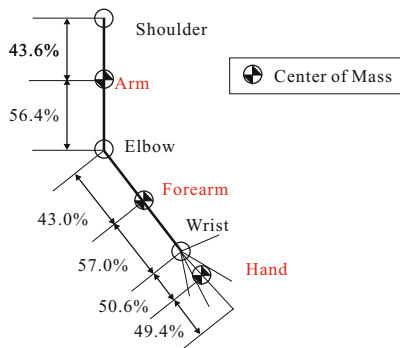


Fig. 3 The distribution of the center of mass (COM) for the human arm segments [41]

The estimation of the mass, the center of mass and the moment of inertia of each arm segment is required to customize the dynamic model for each subject. Figure 3 shows the distribution of the center of mass (COM) for the human arm segments. On average, the human arm contributes 4.8% of the total body weight. The mass of arm segments and their inertia matrices are calculated based on the weight of subjects according to the regression equations in [30].

3 Swivel Angle Estimation for Reaching Movements

3.1 Criterion I: Swivel Angle Estimation Using a Biologically-Based Kinematic Constraint

Given the role of the head as a cluster of sensing organs and the importance of arm manipulation to deliver food to the mouth, we hypothesize that the swivel angle is determined by the human motor control system to efficiently retract the hand to the head region. This hypothesis is supported by intracortical stimulation experiments that evoked coordinated forelimb movements in conscious primates [10][33]. It has been reported that each stimulation site produced a stereotyped posture in which the arm moved to the same final position regardless of its posture in the initial stimulation. In the most complex example, the monkey formed a frozen pose with the hand in a grasping position in front of the open mouth. This implies that during the arm movement toward an actual target, the virtual target point at the head can be set for the potential retraction of the palm to the virtual target as shown in Figure 4.

Manipulability Ellipsoid: According to the above notion of efficient arm movements toward a virtual target at the head, the redundancy of the human arm can be closely associated with the manipulability ellipsoid. Let P_m denote the virtual target position at the center of the head in Figure 5(a). When we consider the combinations of joint velocities satisfying the condition in which $\sum_{i=1}^n \dot{\theta}_i^2 = 1$, the hand velocity as a function of the joint velocity is described by an ellipsoid that defines the arm’s scaled Jacobian. The longest principle axis of the manipulability ellipsoid (i.e., the major principle axis) defines the direction of the highest sensitivity where the end effector velocity varies in response to the joint space velocity (see Figure 5(b)) [28]. Assuming that the virtual hand movement follows the shortest path connecting P_w to P_m , the swivel angle is chosen such that the projection of the major principle axis of the manipulability ellipsoid onto $(P_m - P_w)$ is maximized.

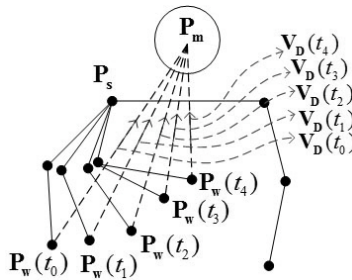


Fig. 4 Virtual destination is at the head, which is a cluster of feedback sensors

Lemma 1. Given the inequality $\|P_w - P_s\| > \|P_w - P_e\|$, the major principle axis of the manipulability ellipsoid is coplanar with plane S , defined by P_w , P_e and P_s , and its magnitude σ_1 is expressed as

$$\sigma_1 = \sqrt{\lambda_1} = \sqrt{((L_{ws}^2 + L_{we}^2) + (L_{ws}^2 + L_{we}^2)c_1)/2} \tag{74}$$

$$c_1 = \sqrt{1 - c_2}, \quad c_2 = 4L_{we}^2 L_{ws}^2 \sin^2 \varphi / (L_{ws}^2 + L_{we}^2)^2$$

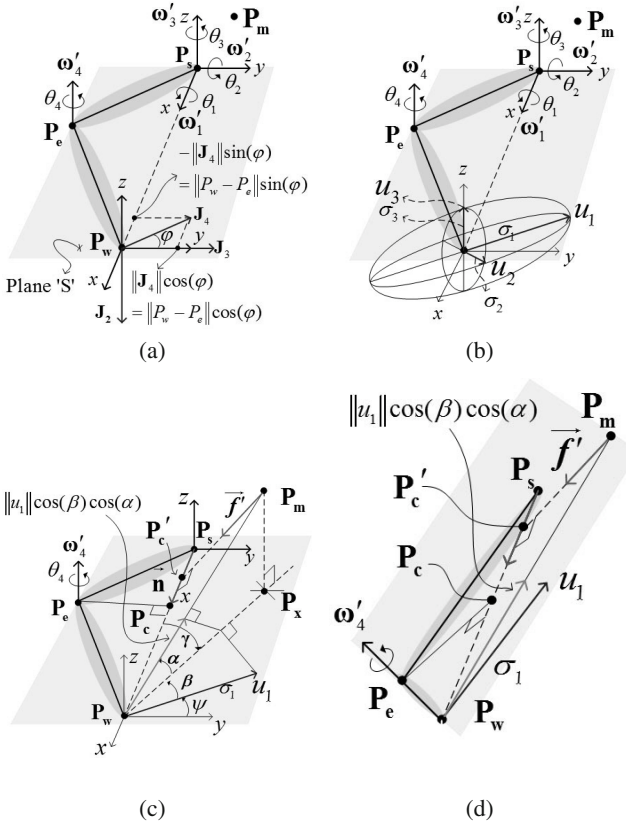


Fig. 5 The new coordinate system composed of P_w, P_e, P_s and P_m . (a) Each element J_i in the Jacobian matrix is defined with respect to the newly defined frame on the shoulder where the x axis is defined as $(P_w - P_s) / \|P_w - P_s\|$ and the y axis sits on the plane S composed of P_w, P_e and P_s . The new frame on the shoulder is defined for the convenience of the calculation. (b) Manipulability ellipsoid at the wrist position. u_1, u_2 and u_3 indicate the three principle axes of the ellipsoid with magnitudes σ_1, σ_2 and σ_3 . (c) The direction of the largest manipulability (i.e., vector u_1) projected on the $(P_m - P_w) / \|P_m - P_w\|$ is marked as an arrow along $(P_m - P_w)$ and its magnitude can be represented as $\|u_1\| \cos(\alpha) \cos(\beta)$. (d) It shows the specific elbow position for the given wrist position that maximizes the manipulability projected on the direction from the hand toward the virtual target. In this configuration, P_m, P_s, P_e and P_w are on the same plane.

Proof. As the human arm moves, the wrist position P_w and elbow position P_e change and therefore a time-varying Plane 'S' can be defined by three points P_s , P_e and P_w . As shown in Figure 5(a), a frame attached to the time-varying Plane S , with its origin located at P_s . The x-axis, denoted by ω_1 , is defined along the vector $|P_w - P_s|$, while the z-axis, denoted by ω_3 , is orthogonal to the plane S . Accordingly, the y-axis, denoted by ω_2 is within the time-varying Plane S . With P_e as the origin of the frame of elbow flexion, θ_4 represents the elbow flexion within the Plane S , with ω_4 as the axis to rotate about.

The relationship between the end-effector velocity $\dot{\mathbf{P}} = [\dot{P}_{wx} \ \dot{P}_{wy} \ \dot{P}_{wz}]^T$ and joint velocity $\dot{\theta} = [\dot{\theta}_1 \ \dot{\theta}_2 \ \dot{\theta}_3 \ \dot{\theta}_4]$ is defined as:

$$\begin{aligned}\dot{\mathbf{P}} &= \mathbf{J}\dot{\theta} = [\mathbf{J}_1 \ \mathbf{J}_2 \ \mathbf{J}_3 \ \mathbf{J}_4]\dot{\theta} \\ &= \mathbf{J}_1\dot{\theta}_1 + \mathbf{J}_2\dot{\theta}_2 + \mathbf{J}_3\dot{\theta}_3 + \mathbf{J}_4\dot{\theta}_4\end{aligned}\quad (75)$$

$$\mathbf{J}_i = \begin{cases} \omega_i \times (P_w - P_s), & i = 1, 2, 3 \\ \omega_i \times (P_w - P_e), & i = 4 \end{cases}\quad (76)$$

Note that $\mathbf{J}_1 = \omega_1 \times (P_w - P_s) = \mathbf{x} \times (P_s - P_w) = 0$. Therefore, we have

$$\dot{\mathbf{P}} = +\mathbf{J}_2\dot{\theta}_2 + \mathbf{J}_3\dot{\theta}_3 + \mathbf{J}_4\dot{\theta}_4\quad (77)$$

With respect to the time-varying Plane S , the attached frame has its x-axis, y-axis, and z-axis in a fixed direction, i.e., $\mathbf{x} = \omega_1 = [1, 0, 0]^T$, $\mathbf{y} = \omega_2 = [0, 1, 0]^T$ and $\mathbf{z} = \omega_3 = [0, 0, 1]^T$. ω_4 is in parallel with ω_3 and therefore we have $\omega_4 = [0, 0, 1]^T$. Using the cross product, the direction of \mathbf{J}_i for $i = 2, 3, 4$ can be determined: \mathbf{J}_2 is in the direction $[0, 0, -1]^T$; \mathbf{J}_3 is in the direction $[0, 1, 0]^T$; the direction of \mathbf{J}_4 is perpendicular to $P_w - P_e$ and ω_4 and therefore in the Plane S , as shown in Figure 5(a). Here, we define the angle between \mathbf{J}_3 and \mathbf{J}_4 as φ . Since all the ω_i s are unit vectors, the magnitude of \mathbf{J}_i can be determined:

$$\|\mathbf{J}_i\| = \begin{cases} \|P_w - P_s\|, & i = 1, 2, 3 \\ \|P_w - P_e\|, & i = 4 \end{cases}\quad (78)$$

Based on the above definitions, we can explicitly express each vector of the Jacobian matrix with respect to the frame attached to Plane S :

$$\mathbf{J}_1 = [0, 0, 0]^T\quad (79)$$

$$\mathbf{J}_2 = \|P_w - P_s\| \cdot [0, 0, -1]^T\quad (80)$$

$$\mathbf{J}_3 = \|P_w - P_s\| \cdot [0, 1, 0]^T\quad (81)$$

$$\mathbf{J}_4 = \|P_e - P_s\| \cdot [-\sin \varphi, \cos \varphi, 0]^T\quad (82)$$

Thus, the Jacobian matrix is:

$$\mathbf{J} = \begin{pmatrix} 0 & 0 & 0 & -L_{we} \sin \varphi \\ 0 & 0 & L_{ws} & L_{we} \cos \varphi \\ 0 & -L_{ws} & 0 & 0 \end{pmatrix} \quad (83)$$

where $L_{ws} = \|P_w - P_s\|$ and $L_{we} = \|P_e - P_s\|$.

By singular value decomposition, we can find $\mathbf{J} = \mathbf{U}\mathbf{\Sigma}\mathbf{V}^T$, where $\mathbf{U} = [u_1, u_2, u_3]^T$, $\mathbf{\Sigma} = \text{diag}(\sigma_1, \sigma_2, \sigma_3)$ and $\mathbf{V} = [v_1, v_2, v_3]^T$. The vectors u_i determine the direction of principle axes of the manipulability ellipsoid, and σ_i determine the radii, as shown in Figure 5(b). By resolving $\det(\mathbf{J}\mathbf{J}^T - \lambda\mathbf{I}) = 0$, we can obtain $\sigma_i = \sqrt{\lambda_i}$. Based on Sarrus's rule, the eigen-values λ_i can be found as:

$$\lambda_{1,2} = \frac{(L_{ws}^2 + L_{we}^2) \pm (L_{ws}^2 + L_{we}^2)c_1}{2}, (\lambda_1 > \lambda_2) \quad (84)$$

$$\lambda_3 = L_{ws}^2 \quad (85)$$

with

$$c_1 = \sqrt{1 - c_2} \quad (86)$$

$$c_2 = \frac{4L_{ws}^2 L_{we}^2 \sin^2 \varphi}{(L_{ws}^2 + L_{we}^2)^2} \quad (87)$$

Note that $0 < c_1 < 1$ and $0 < c_2 < 1$ and therefore $\lambda_{1,2}$ are not complex numbers. Knowing that $\lambda_1 > \lambda_2$, the following proof will show $\lambda_1 > \lambda_3$ and therefore the eigen-vector u_1 corresponding to λ_1 is the longest eigen-vector.

case1: $L_{ws} \geq L_{we}$

$$\begin{aligned} \lambda_1 - \lambda_3 &= \frac{(L_{ws}^2 + L_{we}^2) + (L_{ws}^2 + L_{we}^2)c_1}{2} - L_{ws}^2 \\ &\geq \frac{(L_{we}^2 - L_{ws}^2) + (L_{ws}^2 + L_{we}^2)c_{min1}}{2} \\ &= \frac{(L_{we}^2 - L_{ws}^2) + (L_{ws}^2 + L_{we}^2)\sqrt{1 - c_{max2}}}{2} \\ &= \frac{(L_{we}^2 - L_{ws}^2) + \sqrt{(L_{ws}^2 + L_{we}^2)^2 - 4L_{ws}^2 L_{we}^2}}{2} \\ &= \frac{(L_{we}^2 - L_{ws}^2) + \sqrt{(L_{ws}^2 - L_{we}^2)^2}}{2} = 0 \end{aligned} \quad (88)$$

where c_{min1} is the minimum of c_1 ; c_{max2} is the maximum of c_2 and

$$c_{max2} = \frac{\max(4L_{we}^2 L_{ws}^2 \sin^2(\varphi))}{(L_{ws}^2 + L_{we}^2)^2} = \frac{4L_{we}^2 L_{ws}^2}{(L_{ws}^2 + L_{we}^2)^2} \quad (89)$$

case2: $L_{ws} < L_{we}$

$$\begin{aligned}
 \lambda_1 - \lambda_3 &= \frac{(L_{ws}^2 + L_{we}^2) + (L_{ws}^2 + L_{we}^2)c_1}{2} - L_{ws}^2 \\
 &\geq \frac{(1 + c_{min1})(L_{ws}^2 + L_{we}^2)}{2} - L_{ws}^2 \\
 &\geq \frac{(L_{ws}^2 + L_{we}^2)}{2} - L_{ws}^2 \\
 &= \frac{(L_{we}^2 - L_{ws}^2)}{2} \geq 0
 \end{aligned} \tag{90}$$

$\lambda_1 > \lambda_3$ for all the possible L_{ws} , corresponding to wrist positions for the reaching movements of the human arm. Thus, we can conclude that the longest eigen-vector of the manipulability ellipsoid is u_1 , corresponding to the largest eigen-value of

$$\sigma_1 = \sqrt{\lambda_1} = \sqrt{((L_{ws}^2 + L_{we}^2) + (L_{ws}^2 + L_{we}^2)c_1)/2} \tag{91}$$

The direction of the longest eigen-vector can be found by:

$$(\mathbf{J} \cdot \mathbf{J}^T)\mathbf{X} = \lambda\mathbf{X} \tag{92}$$

where $\mathbf{X} = [x_1, x_2, x_3]^T$.

$$(\mathbf{J} \cdot \mathbf{J}^T)\mathbf{X} = \begin{pmatrix} L_{we}^2 \sin^2 \varphi & -L_{we}^2 \cos \varphi \sin \varphi & 0 \\ -L_{we}^2 \cos \varphi \sin \varphi & L_{ws}^2 + L_{we}^2 \cos^2 \varphi & 0 \\ 0 & 0 & L_{ws}^2 \end{pmatrix} \begin{pmatrix} x_1 \\ x_2 \\ x_3 \end{pmatrix} = \lambda_1 \begin{pmatrix} x_1 \\ x_2 \\ x_3 \end{pmatrix} \tag{93}$$

Therefore

$$\begin{aligned}
 (L_{we}^2 \sin^2 \varphi - \lambda_1)x_1 &= L_{we}^2 \cos \varphi \sin \varphi x_2 \\
 L_{we}^2 \cos \varphi \sin \varphi x_1 &= (L_{ws}^2 + L_{we}^2 \cos^2 \varphi - \lambda_1)x_2 \\
 L_{ws}^2 x_3 &= \lambda_1 x_3
 \end{aligned} \tag{94}$$

For the solution, we have

$$\begin{aligned}
 x_1 &= x_1 \\
 x_2 &= -\frac{\lambda_1 - L_{we}^2 \sin^2 \varphi}{L_{we}^2 \cos \varphi \sin \varphi} x_1 \\
 x_3 &= 0
 \end{aligned} \tag{95}$$

Due to the joint limit, $0^\circ < \varphi < 90^\circ$. When $\varphi = 0^\circ$, the arm is fully extended and therefore at its singular position; $\varphi = 90^\circ$ cannot be achieved since upper and the lower arms can not fully overlap each other.

Note that

$$\begin{aligned}
\lambda_1 - L_{we}^2 \sin^2 \varphi &= \frac{(L_{ws}^2 + L_{we}^2) + (L_{ws}^2 + L_{we}^2)c_1 - 2L_{we}^2 \sin^2 \varphi}{2} \\
&= \frac{(L_{ws}^2 + L_{we}^2) + (L_{ws}^2 + L_{we}^2) \sqrt{1 - \frac{4L_{ws}^2 L_{we}^2 \sin^2 \varphi}{(L_{ws}^2 + L_{we}^2)^2}} - 2L_{we}^2 \sin^2 \varphi}{2} \\
&\geq \frac{(L_{ws}^2 + L_{we}^2) + (L_{ws}^2 + L_{we}^2) \sqrt{1 - \frac{4L_{ws}^2 L_{we}^2}{(L_{ws}^2 + L_{we}^2)^2}} - 2L_{we}^2 \sin^2 \varphi}{2} \\
&= \frac{(L_{ws}^2 + L_{we}^2) + \|L_{ws}^2 - L_{we}^2\| - 2L_{we}^2 \sin^2 \varphi}{2} \\
&= \frac{(L_{ws}^2 - L_{we}^2) + \|L_{ws}^2 - L_{we}^2\| + 2L_{we}^2 \cos^2 \varphi}{2} \\
&\geq \frac{2L_{we}^2 \cos^2 \varphi}{2} = L_{we}^2 \cos^2 \varphi \geq 0
\end{aligned} \tag{96}$$

With $0 < \cos \varphi \leq 1$ and $0 \leq \sin \varphi < 1$,

$$-\frac{\lambda_1 - L_{we}^2 \sin^2 \varphi}{L_{we}^2 \cos \varphi \sin \varphi} x_1 \leq -\frac{L_{we}^2 \cos^2 \varphi}{L_{we}^2 \cos \varphi \sin \varphi} = -\frac{1}{\tan \varphi} < 0 \tag{97}$$

The direction of u_1 is as shown in Figure 5(c).

Optimization of Swivel Angle Using Movement Efficiency: The control of the extra DOF in the human arm, specified by the swivel angle ϕ , can be optimized for best movement efficiency. The proposed biologically-based hypothesis considers the human head (particularly the position of human mouth) as the virtual target for human arm movements. Thus, an optimum swivel angle can be determined such that the projection of the major principle axis u_1 on the vector $P_m - P_w$ is maximized for a given wrist position, since in the direction of the major principle axis, the Jacobian matrix provides the most efficient mapping from joint space velocity to task space velocity.

$$\begin{aligned}
\phi &= \arg \max_{\alpha, \beta \in [0, \pi/2]} [u_1^T (P_m - P_w)] \\
&= \arg \max_{\alpha, \beta \in [0, \pi/2]} [\|u_1\| \|P_m - P_w\| \cos(\alpha) \cos(\beta)]
\end{aligned} \tag{98}$$

By Equation (98), the brute force method is used to explore all the possible swivel angles for a wrist position, to determine the optimum swivel angle. Figure 5(c) demonstrates the geometry of finding the projection of u_1 on $P_m - P_w$. In Figure 5(c), α denotes the angles between $(P_m - P_w)$ and plane S ; β denotes the angle between u_1 and the projection of $(P_m - P_w)$ onto S . The component of u_1 projected onto $(P_m - P_w)$ is represented by $\|u_1\| \cos(\alpha) \cos(\beta)$, marked by the green arrow. It is expected that Equation (98) is maximized when $\alpha = 0^\circ$, regardless of the

β determined by the given wrist position; when $\alpha = 0^\circ$, plane S is coplanar with the plane composed by P_m, P_s and P_w , as shown in Figure 5(d). The optimum swivel angle following the proposed hypothesis can be determined given the positions of P_m, P_w and P_s . Define $\mathbf{f} = P_w - P_m$ and \mathbf{f}' to be the projection of \mathbf{f} on the direction of $P_w - P'_c$. Since \mathbf{f}' is parallel to vector $P_e(\phi) - P_c$ when $\alpha = 0^\circ$, the optimum swivel angle is estimated as:

$$\phi_{kin} = \arctan 2(\mathbf{n} \cdot (\mathbf{f}' \times \mathbf{u}), \mathbf{f}' \cdot \mathbf{u}) \quad (99)$$

This algorithm provides a real-time estimate of the swivel angle and therefore a real-time solution to the inverse kinematics of the human arm. The performance of the ϕ_{est} estimation has been evaluated in [24] and compared to a dynamic model in [23]. This chapter intends to examine this algorithm (referred to as **Criterion I** in the following section) in a more general experimental setup, in comparison with another swivel angle estimation algorithm which addresses the effect of the dynamics of the human arm.

3.2 Criterion II: Swivel Angle Estimation by a Dynamic Constraint

According to [24], the biologically-based swivel angle estimation algorithm using purely kinematic constraints can provide a good estimation. However, the effect of dynamics on human arm movements cannot be underestimated. [23] integrates a dynamic criterion in order to provide an improved estimation of swivel angles and to reveal the effect of the dynamics on human arm movements. The dynamic criterion, proposed in [21] and referred to as **Criterion II** in the following sections, resolves the inverse kinematics by minimizing the magnitude of total work done by joint torques for each time step. It has generated satisfactory predictions of the joint space trajectory for the fundamental motions of the human arm, such as shoulder adduction/abduction, shoulder flexion/extension, shoulder internal/external and elbow flexion/extension. Note that there exist other dynamic criteria which can also be used to improve the estimation performance.

Optimization of Swivel Angles by Minimizing Work in Joint Space: For reaching movements in a 3D workspace, the wrist position of the human arm can be uniquely defined by three variables in the task space, while in the joint space there are four joint angles (three for the shoulder motion and one for the elbow motion) available for configuration. Accordingly, the relationship between movements and muscle forces in a musculoskeletal model is based on the four dynamic equations [21]:

$$T = M\ddot{Q} + C(Q, \dot{Q}) + G(Q) \quad (100)$$

In Equation (100), $\ddot{Q} = [\ddot{q}_1, \ddot{q}_2, \ddot{q}_3, \ddot{q}_4]$ and $\dot{Q} = [\dot{q}_1, \dot{q}_2, \dot{q}_3, \dot{q}_4]$, where q_i represents the joint angle for the i -th DOF. M , $C(Q, \dot{Q})$ and $G(Q)$ represent the matrix of the

moment of inertia, the centrifugal/coriolis forces and the gravity force respectively. The external force is represented by E and this is regarded as zero in this paper since the given task does not involve interacting with an external load. The active and passive joint torque rendered by musculotendinous forces are represented by T . The calculation of work in the joint space for each time step depends on (1) the joint torques and (2) the difference in joint angles. Therefore, the work in the joint space during the movement interval $[t_k, t_{k+1}]$ can be computed for two different conditions. The dynamic constraint adopted in this chapter is from the original work done by [30]. Here, we briefly include the essential parts of the algorithm for the integrity of the chapter.

if $T_{i,t_k} \cdot T_{i,t_{k+1}} > 0$,

$$W_i = \frac{(T_{i,t_k} + T_{i,t_{k+1}}) \cdot \Delta q_i}{2} \quad (101)$$

where T_{i,t_k} and $T_{i,t_{k+1}}$ are the joint torques of the i -th joint at the time t_k and t_{k+1} . $\Delta q_i = (q_{i,t_{k+1}} - q_{i,t_k})$ is the difference of the i -th joint angle during the time interval $[t_k, t_{k+1}]$.

When $T_{i,t_k} \cdot T_{i,t_{k+1}} < 0$,

$$W_i = \frac{(|\Delta q_i| - h_i) \cdot T_{i,t_{k+1}}}{2} - \frac{h_i \cdot T_{i,t_k}}{2} \quad (102)$$

where $h_i = (|T_{i,t_k}| \cdot |\Delta q_i|) / |T_{i,t_{k+1}} - T_{i,t_k}|$ and denotes the difference of the i -th joint angle from q_{i,t_k} to the value corresponding to zero crossing of joint torque.

To minimize the work done in joint space at each time step (E.g. $|W|_{t_k, t_{k+1}}$ for the time interval $[t_k, t_{k+1}]$), the swivel angle of the human arm for a specified wrist position is optimized by the following cost function:

$$C = |W|_{t_k, t_{k+1}} = \sum_{i=1}^4 |W_i|_{t_k, t_{k+1}} \quad (103)$$

where $|W_i|_{t_k, t_{k+1}}$ denotes the work done by the i -th joint.

4 Experiments

4.1 Experiment Setup

3D Spherical Workspace: A 3D spherical workspace is set up in order to examine the swivel angle estimation performance of the above two criteria in more general conditions. This spherical workspace, with its center denoted by the green point in Figure 6, is calculated as a part of the surface of a virtual sphere. The calculated target locations, denoted by blue marks, fall within a red circle, whose size is limited by the width of the back frame of the experiment table. By varying the radius of the virtual sphere, the spherical workspace can be resized, resulting in a new distribution

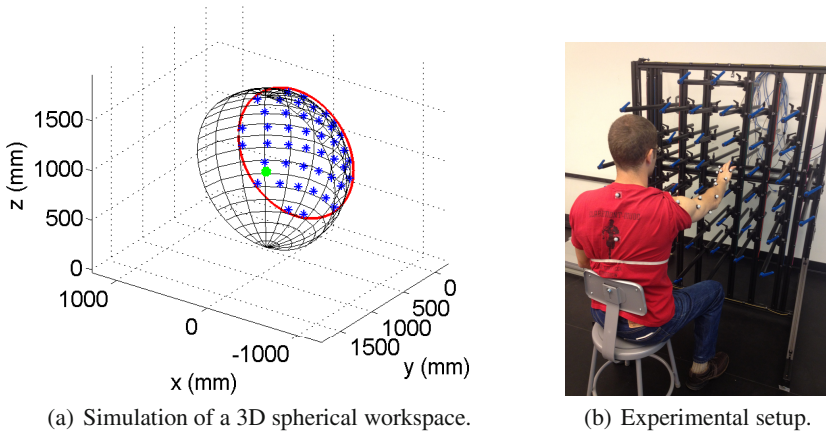


Fig. 6 3D spherical workspace: (a) targets (shown as blues points) are arranged on the surface of a virtual sphere, the center of which is shown as the green point; (b) the spherical workspace is installed on the back frame of a table customized for reaching and grasping experiments

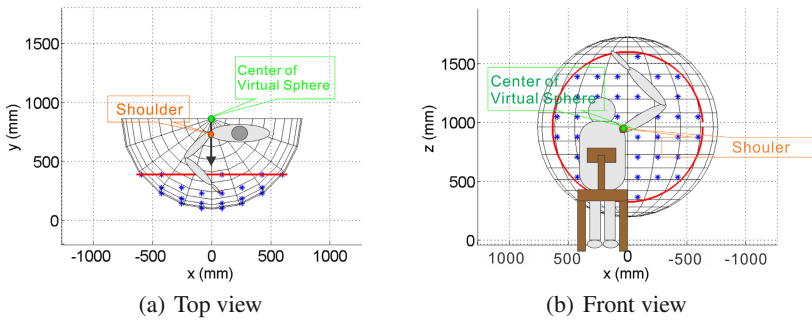


Fig. 7 Experiment setup for reaching movements in a 3D spherical workspace

of target locations and a different target density. The spherical workspace is installed on the back frame of an experiment table customized for reaching and grasping experiments.

To maximize the use of the back frame of the experiment table, this experiment allocates the radius of the virtual sphere to be slightly larger than the width of the back frame. The origin of the virtual sphere (as well as the shoulder of the subject) is equidistant between the left and right boundaries of the frame (Figure 7(a)). With an adjustable chair, the right shoulder of a subject can be aligned at the height of the center of the virtual sphere. As shown in Figure 7(b), the center of the virtual sphere and the shoulder of the subject overlap in the front view.

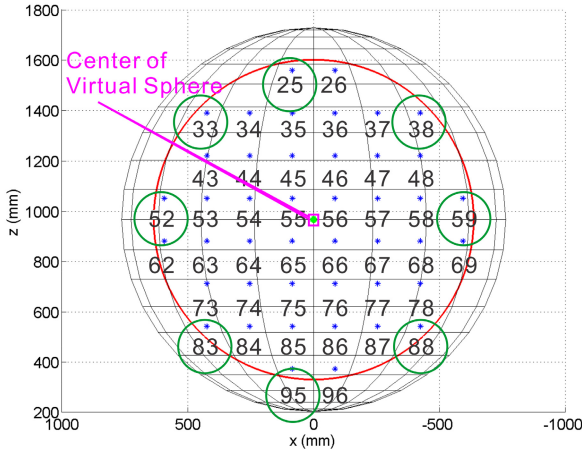


Fig. 8 Targets involved in reaching experiments, marked by green circles

The spherical workspace is evenly discretized and 44 targets are allocated with the same interval in both the vertical direction (i.e. along the z-axis) and the horizontal direction (i.e. along the x-axis). Each target is numbered by its row and column.

Subjects: This experiment involves five healthy volunteer right-handed subjects (three males and two females; age range 22-38 years old; average age 28 years old) without any clinical symptoms or any history of motor, sensory or neurological disorders. The subjects are naive as to the purpose the experiment, and are only instructed to perform point to point reaching movements in a naturally self-paced way.

Experiment Protocol: In this experiment, subjects are expected to conduct eight sessions of reaching movements with their right arms. The targets involved in this experiment are 25, 33, 38, 52, 59, 83, 88, and 96, as shown in Figure 8. Each of the eight sessions chooses an involved target to be the destination (i.e. the end target) of the reaching movements for the whole session. In each session, a subject iteratively starts from one of all the other involved targets and reaches to the end target of that session, according to the trial sequence denoted in Equation (104). Each session consists of five repetitions of seven different reaching movements (35 trials in total).

$$\begin{aligned}
 & \left\{ \begin{array}{l}
 \text{Session 1 : } 33 \rightarrow 25, 38 \rightarrow 25, 52 \rightarrow 25, 59 \rightarrow 25, 83 \rightarrow 25, 88 \rightarrow 25, 96 \rightarrow 25 \\
 \text{Session 2 : } 25 \rightarrow 33, 38 \rightarrow 33, 52 \rightarrow 33, 59 \rightarrow 33, 83 \rightarrow 33, 88 \rightarrow 33, 96 \rightarrow 33 \\
 \text{Session 3 : } 25 \rightarrow 38, 33 \rightarrow 38, 52 \rightarrow 38, 59 \rightarrow 38, 83 \rightarrow 38, 88 \rightarrow 38, 96 \rightarrow 38 \\
 \text{Session 4 : } 25 \rightarrow 52, 33 \rightarrow 52, 38 \rightarrow 52, 59 \rightarrow 52, 83 \rightarrow 52, 88 \rightarrow 52, 96 \rightarrow 52 \\
 \text{Session 5 : } 25 \rightarrow 59, 33 \rightarrow 59, 38 \rightarrow 59, 52 \rightarrow 59, 83 \rightarrow 59, 88 \rightarrow 59, 96 \rightarrow 59 \\
 \text{Session 6 : } 25 \rightarrow 83, 33 \rightarrow 83, 38 \rightarrow 83, 52 \rightarrow 83, 59 \rightarrow 83, 88 \rightarrow 83, 96 \rightarrow 83 \\
 \text{Session 7 : } 25 \rightarrow 88, 33 \rightarrow 88, 38 \rightarrow 88, 52 \rightarrow 88, 59 \rightarrow 88, 83 \rightarrow 88, 96 \rightarrow 88 \\
 \text{Session 8 : } 25 \rightarrow 96, 33 \rightarrow 96, 38 \rightarrow 96, 52 \rightarrow 96, 59 \rightarrow 96, 83 \rightarrow 96, 88 \rightarrow 96
 \end{array} \right. \\
 & 5 \text{ repeats} \times \left. \begin{array}{l} \\ \\ \\ \\ \\ \\ \\ \\ \end{array} \right\} \tag{104}
 \end{aligned}$$

During the experiment, a subject sits in a chair with a straight back support. The placement of the chair enables the subject to point at the targets with comfort and with his/her elbow flexed to roughly 90° (as shown in Figure 6(b)). The height of the chair is adjustable such that the right shoulder of the subject is aligned with the height of the center of the spherical workspace. The right arm is free for pointing movements, but the body of the subject is bounded to the chair back, in order to minimize shoulder displacement. During the pointing movements, the subject is asked to keep the pointing finger in line with the forearm to minimize wrist flexion.

The subjects are instructed to point with the tip of the index finger at their own paces. At the beginning of each trial, a subject is informed of the targets that the trajectory starts with and ends at, i.e., the start target and end target. After receiving a "start" command, the subject points his/her index finger from the start target to the end target.

A motion capture system records an individual file for each trial, starting from the time when the subject puts his/her index finger on the start target and ending after the index finger becomes steady at the end target. To avoid the effect of fatigue, the subject can take a rest after completing each session and can take a rest during a session if he/she feels like it.

5 Results and Discussion

This section presents the results of the swivel angle estimation based on different criteria, and compares them with the measurements of swivel angles from the reaching experiment. The performance of different swivel angle estimation algorithms is evaluated and compared using their estimation errors at targets and during movements.

Figure 9 provides an example of the swivel angle profiles of a subject reaching between two targets: moving forward from Target 1 to Target 7, and moving backward from Target 7 to Target 1. Note that when the measured swivel angle (the blue lines in Figure 9), which denotes the arm postures of the subject in the experiment, is approximately symmetric for moving forward and backward between the two targets. This symmetry of the arm postures is better addressed in the swivel estimation by Criterion I (the green lines), than that by Criterion II.

Section 5.1 examines the swivel angle profiles of all the trials for each subject. The experimentally measured swivel angle demonstrates posture consistency for each individual subject, i.e. the same subject tends to use the same arm posture (measured by the swivel angle) to reach for a target, regardless of whether the subject is moving toward or moving away from the target. In addition, reaching movements are symmetric when comparing the profiles of measured swivel angles for the reaching movements between the same two targets and in opposite directions. The posture consistency and trajectory symmetry are related. Particularly, the posture consistency is an important characteristic of human arm movements, such that the swivel angle estimation of a good control strategy for human arm movements should be able to address it.

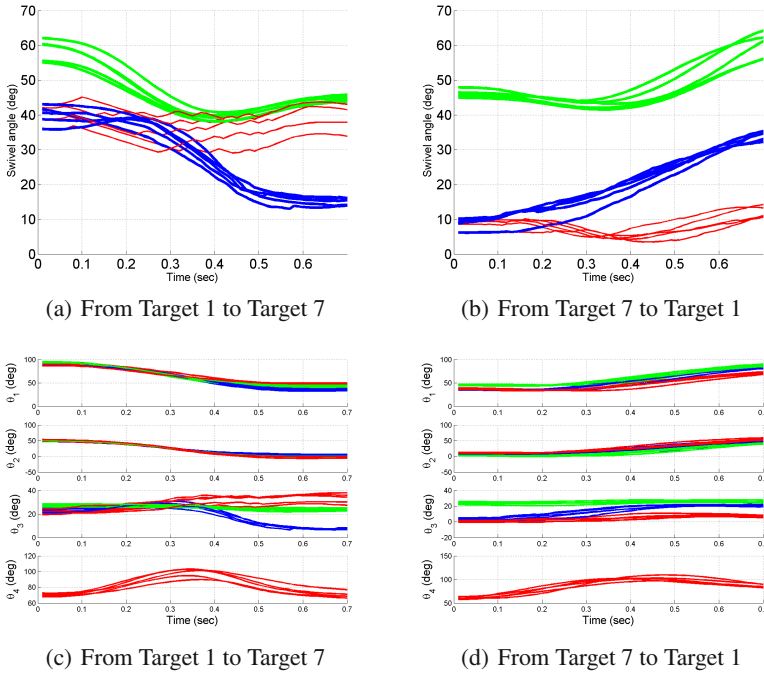


Fig. 9 Figure 9(a) and Figure 9(b) show the experimentally measured swivel angle profiles and the estimated swivel angle profiles by different criteria; Figure 9(c) and Figure 9(d) are the profiles of joint angles correspondingly. In all the figures, the blue lines are the measured swivel angle profiles, the green lines are the profiles of the swivel angle estimated based on criterion I (the efficiency of arm movement), and the red lines are the profiles of swivel angle estimated based criterion II (minimizing work in the joint space).

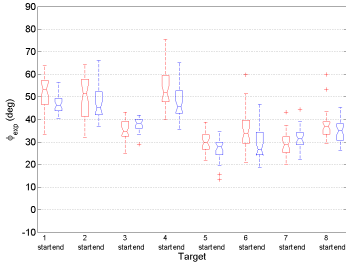
5.1 Posture Consistency in Human Arm Movements

Posture Consistency: The Regularity in Human Arm Movements: Posture consistency is an interesting characteristic of human arm movements. Without any specific instructions or manipulation intentions, a subject moving his/her arm in free space tends to use the same arm posture to reach the same position, regardless of whether the subject is moving toward or away from the target.

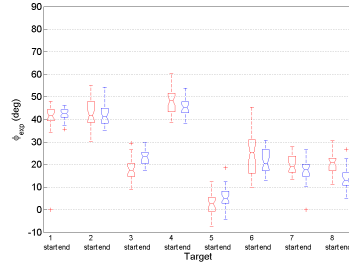
Posture consistency is important because it implies that for reaching movements in a free space, a unique redundancy resolution corresponding to a unique arm posture is associated with each wrist position. Among all the hypotheses of control strategies for human arm movements, a control strategy that addresses posture consistency can be systematically adjusted to achieve improved estimation accuracy, while control strategies that do not address posture consistency may not represent the characteristics of human arm movements.

To study the arm postures at each target, we define the swivel angle that a subject takes when he/she moves away from the target as the "start posture", and the swivel angle that a subject takes when he/she moves toward the target as the "end posture". Figure 10 presents the statistics of target postures for each subject, showing that at each target the start and the end postures are very close to each other.

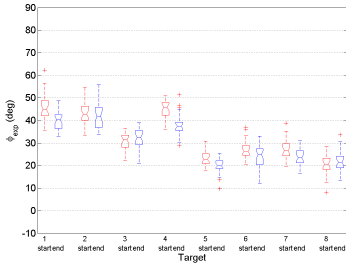
Figure 11 shows the statistics of averaged posture differences measured during the experiment for each subject. The averaged posture difference $\|\phi_{start} - \phi_{end}\|$ is computed for each involved target, as the difference between the averaged start



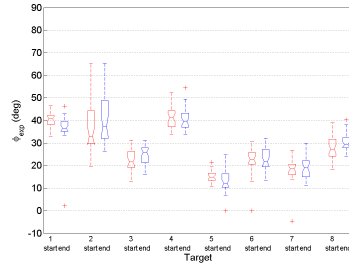
(a) Subject 1.



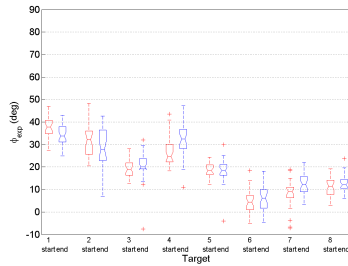
(b) Subject 2.



(c) Subject 3.



(d) Subject 4.



(e) Subject 5.

Fig. 10 Swivel angle difference between the start and the end postures

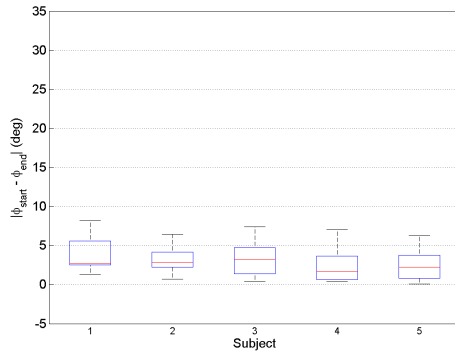


Fig. 11 Posture consistency measured in the experiments. Each subject had a median average posture difference of less than 5° across all targets, and the maximum average posture difference was less than 10° for any target.

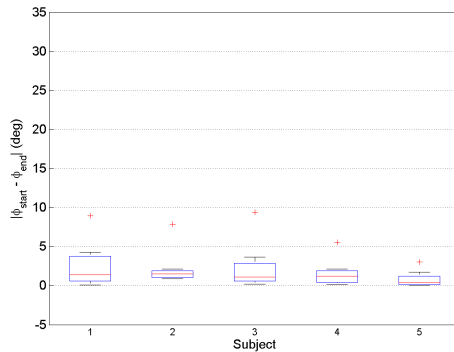


Fig. 12 Posture consistency by Criterion I. Each subject had a median average posture difference of less than 3° across all targets, and the maximum average posture difference was less than 5° for any target.

posture at a target and the averaged end posture at the same target. As shown in Figure 11, all subjects have a median of the averaged posture difference (across all targets) of less than 5°, and the maximum of the averaged posture difference for any target was less than 10°.

The average posture difference can also be calculated for the estimated target postures according to the different estimation criteria. The average predicted posture differences for each subject are generally smaller in Figure 12 than in Figure 13. It can be concluded that posture consistency is addressed better by Criterion I than by Criterion II. Under Criterion I all subjects have a median of the averaged posture difference less than 3°, and the maximum of the averaged posture difference across all subjects is less than 5°, while using Criterion II all subjects have a median of the

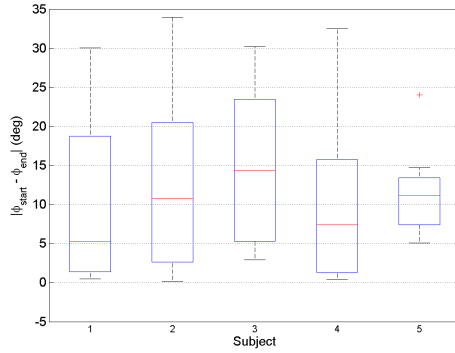


Fig. 13 Posture consistency by Criterion II. Each subject had a median average posture difference of less than 15° across all targets, and the maximum average posture difference was less than 35° for any target.

averaged posture difference less than 15°, and the maximum of the averaged posture difference is less than 35°. Criterion I has a better performance than Criterion II on posture consistency.

Analysis of Systematic Errors in Swivel Angle Estimation: Figure 14 demonstrates the systematic error in swivel angle estimation by different criteria, and for start and the end posture, respectively. ϕ_{exp} is the average swivel angle measured in the experiment, while ϕ_{est} and ϕ_{dyna} are the average swivel angle estimated by Criterion I and Criterion II, respectively. Note that the perfect posture consistency demonstrated in Figure 14(b) is because Criterion II intentionally uses the measured swivel angle as the initial value to start its estimation.

Both Figure 14(a) and Figure 14(c) show that the systematic error of swivel angle estimation based on Criterion I can be related to the horizontal position of targets with respect to shoulder location. In general, Criterion I tends to overestimate the swivel angle and therefore expects higher elbow position than the experimental measurements; however, given targets of the same height, the overestimation is more significant for targets to the left of the shoulder than for the targets to the right of the shoulder. Note that in the workspace, target 3, 5 and 7 (called "right targets") are to the right of shoulder, target 2, 4, 6 (called "left targets") are to the left of shoulder, and target 1 and 8 (called "middle targets") are aligned with the shoulder. The systematic overestimation related to the horizontal position of the targets can be found by comparing target postures at the left target and at right target of the same height in pairs (e.g., target 2 VS target 3, target 4 VS target 5; and target 6 VS target 7). Note that the arm postures at target 1 are more overestimated than at target 8.

The systematic estimation error of Criterion I may be explained by the following fact: when reaching to the targets to the right of shoulder, the right arm moves in free space and therefore the effect of gravity is more significant, while reaching to the targets to the left of the shoulder, the movements of right arm will be blocked

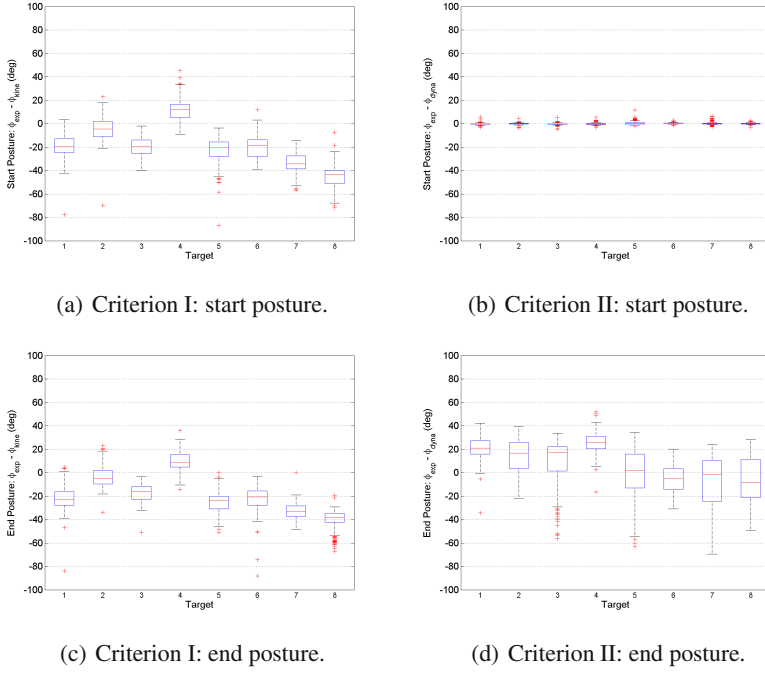


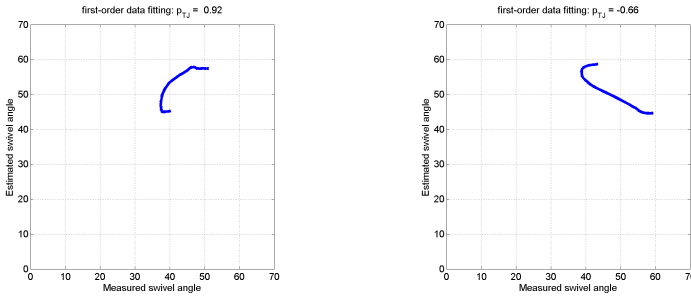
Fig. 14 Systematic error in swivel angle estimation for different criteria

by the torso and the lap. The effect of gravity is partially countered by the force produced by joint limits and workspace constraints.

In general, Criterion II tends to underestimate the swivel angle and expect lower elbow positions compared to those measured in the experiments. Figure 14(d) shows that the underestimation of swivel angles is related to the heights of targets with respect to the height of the shoulder, targets 1, 2, and 3 (called "higher targets") are above the shoulder, targets 6, 7, and 8 (called "lower targets") are below the shoulder, and targets 4 and 5 (called "middle targets") are aligned at the same height as the shoulder. In Figure 14(d), it is shown that the swivel angles at the higher targets and middle target 4 are more underestimated, while the lower targets and middle target 5 may be slightly underestimated, with the estimated swivel angles close to measured swivel angles.

5.2 Estimation Error during Reaching Movements

As noted in the experimental protocol, each subject conducted five repeats of each trajectory (i.e. reaching movements starting from the same target and ending at the same target). The estimation performance of different criteria are further evaluated by the standard deviation of estimation errors during the movements.



(a) Good swivel angle estimation. (b) Bad swivel angle estimation.

Fig. 15 Example of the different performance of swivel angle estimation. p_{TJ} is calculated by first-order regression to represent how well the estimated swivel angle fits the measured swivel angle along a trajectory. In (a) $P_{TJ} = 0.92$, indicating the estimated swivel angle fits the measured swivel angle well; in (b) $P_{TJ} = -0.66$, indicating the estimated swivel angle does not fit the measured swivel angle.

Figure 15 shows examples of evaluating the performance of a criterion on the swivel angle estimation along a trajectory. For different trajectories created by the same subject, the same criterion may produce swivel angle estimations that are better for some trajectories than for others. The evaluation of estimation performance is conducted by linear regression of the estimated swivel angle versus the measured swivel angle along a trajectory. The slope of linear regression (p_{TJ}) shows how much the estimated swivel angle fits the measured swivel angle. In the best case, the slope of linear regression is supposed to be 1, indicating that the estimated swivel angle fits the measured swivel angle all along the trajectory.

As shown in Figure 16, all the trajectories of reaching movements are further categorized by the slope p_{TJ} of the first order regression of the measured swivel angles with respect to the estimated swivel angles along a trajectory. In Figure 16, the targets are numbered in sequence and trajectories are denoted by colored vectors: trajectories with $p_{TJ} < -0.6$ are in red; trajectories with $p_{TJ} > 0.6$ are in green; and trajectories with $0.6 < p_{TJ} < 0.6$ are in yellow. The estimation performance at each target, measured by \overline{MEAN}_{Target} and calculated by averaging the absolute values of the estimation errors at a target, are also categorized and marked by different colors.

The targets with $\overline{MEAN}_{Target} < 10^\circ$ are green, the targets with $\overline{MEAN}_{Target} > 20^\circ$ are red, and the targets with $10^\circ < \overline{MEAN}_{Target} < 20^\circ$ are yellow. By comparing the estimation performance of the two criteria, it can be found that Criterion II outperforms Criterion I, indicating that the control strategy for human arm movements has is linked to energy, which is mostly related to the effect of gravity. Therefore, a pure kinematic model such as Criterion I can not estimate the swivel angle very well by itself. On the other hand, the estimation performance of Criterion I shows the blocking effect of the human body on human arm movements, particularly for the trajectories with poor swivel angle estimation (the cluster on the left side of the workspace, mostly related to Target 4). (Note that when reaching to Target 4, the

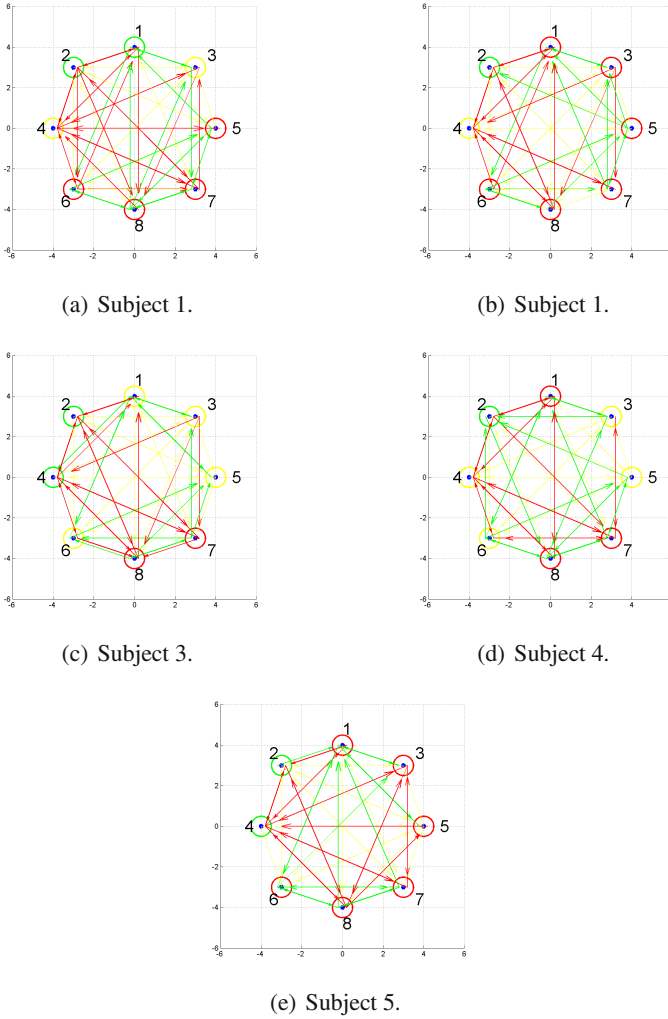


Fig. 16 Criterion I: categorization of reaching movement trajectories by estimation performance. The performance of estimation is evaluated by the slope p_{TJ} of the first order regression between measured swivel angles and estimated swivel angles along a trajectory. Colored vectors connecting targets denote the corresponding trajectories of movements: trajectories with $p_{TJ} < -0.6$ are in red; trajectories with $p_{TJ} > 0.6$ are in green; and trajectories with $0.6 < p_{TJ} < 0.6$ are in yellow. The estimation performance at each target, measured by \overline{MEAN}_{Target} and calculated by averaging the absolute values of estimation errors at a target, are also categorized and marked by different colors: the targets with $\overline{MEAN}_{Target} < 10^\circ$ are green, the targets with $\overline{MEAN}_{Target} > 20^\circ$ are red, and the targets with $10^\circ < \overline{MEAN}_{Target} < 20^\circ$ are yellow.

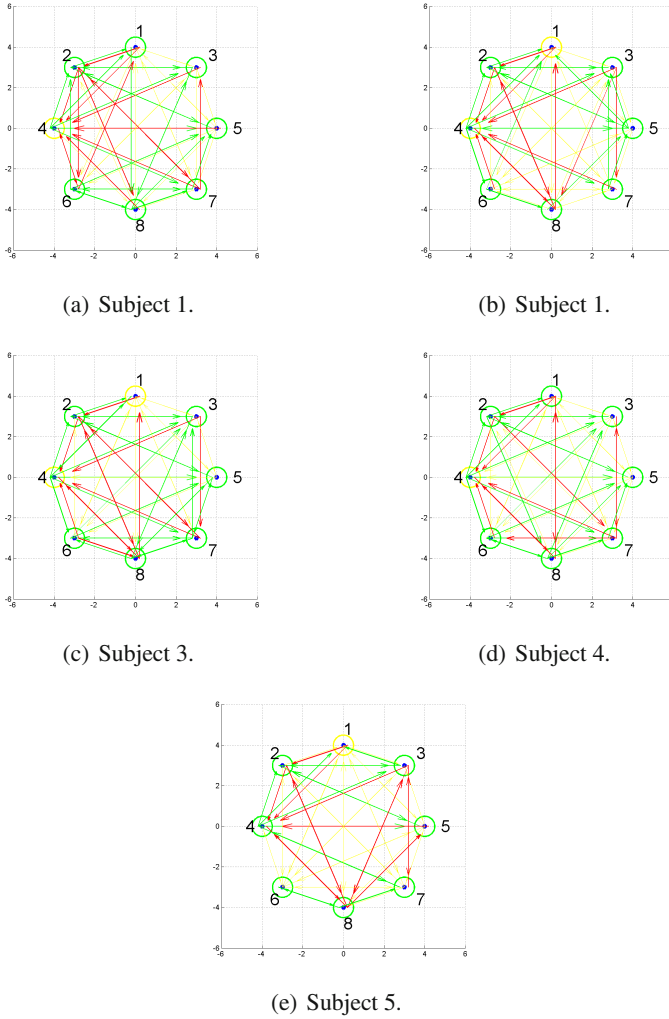


Fig. 17 (Continue Figure 16) **Criterion II:** categorization of reaching movement trajectories by estimation performance

right human arm is blocked by torso to the largest extent.) The estimation performance of Criterion I also demonstrates the effect of gravity, since the poor estimation of target posture happens for the lower targets on the right of the workspace (i.e. Target 5 and Target 7). There, the human arm moves in free space, and the measured swivel angles are much lower than the estimated swivel angles.

Comparing Figure 16 and Figure 17, Criterion II demonstrates a better performance for the estimation of arm postures at targets and along trajectories. This experimental result may seem to contradict the results of [23], in which Criterion I provided a better swivel angle estimation than Criterion II. However, this apparent contradiction can be explained by the difference in the experimental protocol. In [23], the targets are on the surface of the table and on frames, and the subjects are asked to touch the targets slightly with their hands. During the experiments, subjects touched the targets with the finger pads of the three middle fingers. The orientation of the hand affected the elbow position and resulted in a larger swivel angle. In addition to the hand orientation, the subjects avoided collision with the table surface and therefore chose higher elbow positions unconsciously. In addition, note that under Criterion II, the swivel angle estimation algorithm takes the measured swivel angle at the start target as an initial condition, which contributes to a higher performance of swivel angle estimation for the whole trajectory. At the same time, Criterion I estimates the initial swivel angle and does not require measuring the initial swivel angle.

6 Conclusion

Posture consistency is an important characteristic of human arm movements. Without intent to manipulate, a subject tends to use the same arm posture to reach the same target in a 3D free space, regardless of whether the subject is moving toward or moving away from the target. This regularity in human arm movements, previously revealed by Donders' law, is confirmed by the experimental data presented in this chapter. The subjects involved in the reaching experiments have their posture difference median at the targets smaller than 5° , and posture difference maximum across all the targets less than 10° . This posture consistency implies that given the kinematic redundancy in the human arm, human motor control chooses a unique arm posture associated with a 3D hand position.

Previously proposed control strategies for controlling the redundant degree of freedom provide different predictions of the arm postures corresponding to the same wrist position in a 3D space. This chapter examined the arm posture predictions of two control strategies: one that maximizes the movement efficiency towards the head, particularly toward the mouth (Criterion I); and the other that minimizes the energy consumption in joint space at each time step (Criterion II). The predictions of arm postures by the two control strategies are compared and the prediction errors for each control strategy are analyzed: posture consistency is a better addressed by Criterion I, while Criterion II has smaller estimation error along the arm movement trajectories and therefore demonstrates better performance when predicting the "movement trend". Further work will evaluate arm posture predictions based on other criteria or based on their combinations to achieve improved arm posture predictions.

References

1. Angeles, J., Lopez-Cajun, C.S.: Kinematic isotropy and the conditioning index of serial robotic manipulators. *Int. J. Robotics Research* 11(6), 560–571 (1992)
2. Angeles, J., Park, F.C.: Performance evaluation and design criteria. In: Siciliano, B., Khatib, O. (eds.) *A Handbook of Robotics*, 1st edn. Springer Handbook of Robotics, pp. 229–244 (2008)
3. Asada, H., Granito, J.: Kinematic and static characterization of wrist joints and their optimal design. In: *Proc. 1985 Int. Conf. Robot. Automat.*, St. Louis, Missouri, pp. 244–250 (March 1985)
4. Badler, N.I., Tolani, D.: Real-time inverse kinematics of the human arm. *Presence* 5(4), 393–401 (1996)
5. Bernstein, N.A.: *The coordination and regulation of movements*. Pergamon Press, Oxford (1967)
6. Bicchi, A.: On the mobility and manipulability of general multiple limb robots. *IEEE Journal of Robotics and Automation* 11(2), 215–228 (1995)
7. Boullion, T.L., Odell, P.L.: *Generalized inverse matrices*. Wiley-Interscience (1971)
8. Craig, J.J.: *Introduction to Robotics: Mechanics and Control*, 3rd edn., ch.1. Prentice Hall (2003)
9. Desmurget, M., Grea, H., Prablanc, C.: Final posture of the upper limb depends on the initial position of the hand during prehension movements. *Current Biology* 119(4), 511–516 (1998)
10. Dum, R., Strick, P.: Motor Areas in the frontal Lobe: The Anatomical Substrate for the Central Control of Movement. In: *Motor Cortex in Voluntary Movements*. CRC Press (2005)
11. Flash, T., Hogan, N.: The coordination of arm movements: an experimentally confirmed mathematical model. *Journal of Neurophysiology* 5, 1688–1703 (1985)
12. *Motion Genesis*. Autolev
13. Gordon, J., Ghilardi, M.F., Ghez, C.: Accuracy of planar reaching movements. *Experimental Brain Research* 99(1), 97–111 (1994)
14. Gosselin, C.M., Angeles, J.: A new performance index for the kinematic optimization of robotic manipulator. In: *Proc. ASME Mec. Conf.*, Kissimmee, FL, pp. 441–447 (1988)
15. Harris, C.M., Wolpert, D.M.: Signal-dependent noise determines motor planning. *Nature* 394, 780–784 (1998)
16. Harwood, M.R., Mezey, L.E., Harris, C.M.: The spectral main sequence of human saccades. *Journal of Neurophysiology*, 19
17. Hausteiner, W.: Considerations on Listing's law and the primary position by means of a matrix description of eye position control. *Biological Cybernetics* 60(6), 411–420 (1989)
18. Hermens, F., Gielen, S.: Posture-based or trajectory-based movement planning: a comparison of direct and indirect pointing movements. *Experimental Brain Research* 159(3), 340–348 (2004)
19. Hogan, N.: An organizing principle for a class of voluntary movements. *Journal of Neuroscience* 4(2), 2745–2754 (1984)
20. Kane, T.R., Levinson, D.A.: *Dynamics: Theory and Applications*. McGraw-Hill, New York (1985)
21. Kang, T., He, J., Helms Tillery, S.I.: Determining natural arm configuration along a reaching trajectory. *Exp. Brain Res.* 167, 352–361 (2005)

22. Kawato, M.: Bidirectional theory approach to integration. In: Inui, T., McClelland, J.L. (eds.) *Attention and Performance XVI: Information Integration in Perception and Communication*, pp. 335–367. The MIT Press, Cambridge (1996)
23. Kim, H., Li, Z., Milutinovic, D., Rosen, J.: Resolving the redundancy of a seven dof wearable robotic system based on kinematic and dynamic constraint. In: *ICRA, St. Paul, Minnesota, USA (2012)*
24. Kim, H., Miller, L., Rosen, J.: Redundancy resolution of a human arm for controlling a seven dof wearable robotic system. In: *IEEE International Conference on EMBC, Boston, USA, August 30-September 3 (2011)*
25. Krebs, H.I., Ferraro, M., Buerger, S. P., Newbery, M.J., Makiyama, A., Sandmann, M., Lynch, D., Volpe, B. T., Hogan, N.: Rehabilitation robotics: pilot trial of a spatial extension for mit-manus. *J. Neuro Engineering & Rehabilitation* (October 2004)
26. Li, Z., Latash, M.L., Zatsiorsky, V.M.: Force sharing among fingers as a model of the redundancy problem. *Experimental Brain Research*, 119
27. Li, Z., Glozman, D., Milutinovic, D., Rosen, J.: Maximizing dexterous workspace and optimal port placement of a multi-arm surgical robot. In: *Proc. IEEE Int. Conf. on Robotics and Automation, Shanghai, China*, pp. 3394–3399 (May 2011)
28. Maciejewski, A.A.: Dealing with the ill-conditioned equations of motion for articulated figures. In: *IEEE Computer Graphics and Applications*, pp. 63–71 (1990)
29. Medendorp, W.P., Crawford, J.D., Henriques, D.Y.P., Van Gisbergen, J.A.M., Gielen, C.C.A.M.: Kinematic strategies for upper arm/forearm coordination in three dimensions. *J. Neurophysiology* 84(5), 2302–2316 (2000)
30. Aerospace medical research laboratory. Investigation of inertial properties of human body. Technical report (March 1975)
31. Messier, J., Kalaska, J.F.: Comparison of variability of initial kinematics and endpoints of reaching movements. *Experimental Brain Research* 125(2), 139–152 (1999)
32. Miller, L.M., Rosen, J.: Comparison of multi-sensor admittance control in joint space and task space for a seven degree of freedom upper limb exoskeleton. In: *Proceedings of the 3rd IEEE RAS & EMBS International Conference on Biomedical Robotics and Biomechanics, Tokyo, Japan*, pp. 26–29 (September 2010)
33. Graziano, M.S., Tylor, C.S., Moore, T.: Complex movements evoked by micro stimulation of precentral cortex. *Neuron* 30, 34(5), 841–851 (2002)
34. Muller, H., Sternad, D.: Motor learning: changes in the structure of variability in a redundant task. *Advances in Experimental Medicine and Biology, Progress in Motor Control* 629, 439–456 (2009)
35. Nakano, E., Imamizu, H., Osu, R., Uno, Y., Gomi, H., Yoshioka, T., Kawato, M.: Quantitative examinations of internal representations for arm trajectory planning: Minimum commanded torque change model. *The Journal of Neurophysiology* 81(5), 2140–2155 (1999)
36. Nelson, W.L.: Physical principles for economies of skilled movements. *Biological Cybernetics*, 46
37. Pandy, M.G., Garner, B.A., Anderson, F.C.: Optimal control of non-ballistic muscular movements: a constraint-based performance criterion for rising from a chair. *Journal of Neurophysiology* 117
38. Perry, J.C., Rosen, J.: Design of a 7 degree-of-freedom upper-limb powered exoskeleton. In: *IEEE/RAS-EMBS International Conference on Biomedical Robotics and Biomechanics, Pisa, Italy (February 2006)*

39. Perry, J.C., Rosen, J., Burns, S.: Upper-limb powered exoskeleton design. *Mechatronics* 12(4), 408–417 (2007)
40. Perry, J.C., Rosen, J., Burns, S.: Upper-limb powered exoskeleton design. *Mechatronics* 12(4), 408–417 (2007)
41. Roberts, S.L., Falkenberg, S.K.: *Biomechanics: Problem Solving for Functional Activity*. St. Louis, Mosby (1992)
42. Rosenbaum, D.A.: *Human Motor Control*. Academic Press (1990)
43. Rosenbaum, D.A., Meulenbroek, R.J., Vaughan, J., Jansen, C.: Posture-based motion planning: applications to grasping. *Psychological Review* 108(4), 709–734 (2001)
44. Sabes, P.N., Jordan, M.I., Wolpert, D.M.: The role of inertial sensitivity in motor planning. *Journal of Neuroscience*, 18
45. Saha, S.K.: *Introduction to Robotics*. Tata McGraw-Hill Publishing Company Limited (2008)
46. Schaal, S., Sternad, D.: Origins and violations of the 2/3 power law in rhythmic 3d movements. *Experimental Brain Research* 136, 60–72 (2001)
47. Schmidt, R.A., Zelaznik, H., Hawkins, B., Frank, J.S., Quinn, J.T.: Motor-output variability: a theory for the accuracy of rapid motor acts. *Psychology Review*, 47
48. Scholz, J.P., Schoner, G.: The uncontrolled manifold concept: identifying control variables for a functional task. *Experimental Brain Research* 126(3), 289–306 (1999)
49. Scholz, J.P., Schoner, G., Latash, M.L.: Identifying the control structure of multijoint coordination during pistol shooting. *Experimental Brain Research* 135(3), 382–404 (2000)
50. Sciavicco, L.: A dynamic solution to the inverse kinematic problem for redundant manipulators. In: *ICRA*, vol. 4, pp. 1081–1087 (March 1987)
51. Sciavicco, L.: A solution algorithm to the inverse kinematic problem for redundant manipulators. *IEEE Journal of Robotics and Automation* 4(4), 403–410 (1988)
52. Smeets, J.B., Brenner, E.: A new view on grasping. *Motor Control* 3, 237–271 (1999)
53. Soechting, J.F., Buneo, C.A., Herrmann, U., Flanders, M.: Moving effortlessly in three dimensions: does donders' law apply to arm movement? *J. Neuroscience* 15(9), 6271–6280 (1995)
54. Soechting, J.F., Flanders, M.: Parallel, interdependent channels for location and orientation in sensorimotor transformations for reaching and grasping. *Journal of Neurophysiology* 70(3), 1137–1150 (1993)
55. Sutton, G.G., Sykes, K.: The variation of hand tremor with force in healthy subjects. *Journal of Physiology*, 191
56. Terzuolo, C.A., Viviania, P.: Determinants and characteristics of motor patterns used for typing. *Journal of Neuroscience* 5, 431–437 (1982)
57. Tillery, S.I., Ebner, T.J., Soechting, J.F.: Task dependence of primate arm postures. *Experimental Brain Research* 104(1), 1–11 (1995)
58. Todorov, E.: Cosine tuning minimizes motor errors. *Neural Computation* 14
59. Todorov, E., Jordan, M.I.: Optimal feedback control as a theory of motor coordination. *Nature Neuroscience* 5, 1226–1235 (2002)
60. Todorov, E., Jordan, M.I.: Smoothness maximization along a predefined path accurately predicts the speed profiles of complex arm movements. *Journal of Neuroscience* 880, 696–714 (1998)
61. Tolani, D., Goswami, A., Badler, N.I.: Real-time inverse kinematics techniques for anthropomorphic limbs. *Graphical Models and Image Processing* 62(5), 353–388 (2000)

62. Uno, Y., Kawato, M., Suzuki, R.: Formation and control of optimal trajectory in human multijoint arm movement - minimum torque-change model. *Biology Cybernetics* 61, 89–101 (1989)
63. Vaillancourt, D.E., Newell, K.M.: movement variability and theories of motor control. In: Latash, M., Zatsiorsky, V. (eds.) *Classics in Movement Science*, pp. 409–435. *Human Kinetics* (2001)
64. Viviani, P., Terzuolo, C.: Trajectory determines movement dynamics. *Journal of Neuroscience* 7, 431–437 (1982)
65. Wada, Y., Kaneko, Y., Nakano, E., Osu, R., Kawato, M.: Quantitative examinations for multi joint arm trajectory planning using a robust calculation algorithm of the minimum commanded torque change trajectory. *Journal of Neural Networks* 14, 381–393 (2001)
66. Woodworth, R.S.: *The Accuracy of Voluntary Movement*. The Macmillan Company (1899)
67. Yoshikawa, T.: Dynamic manipulability of robot manipulators. In: *Proc. Int. Conf. Robot. Automat.*, St. Louis, Missouri, pp. 1033–1038 (March 1985)
68. Yoshikawa, T.: *Foundations of Robotics: Analysis and Control*. The MIT Press (1990)